

# Mechanical properties and deformation behaviour of highly porous pure titanium structures

---

A FIRST STEP TOWARDS THE DESIGN OF A PLASTICALLY DEFORMABLE ACETABULAR IMPLANT



Annemiek Groenewoud

January 2018





# Mechanical properties and deformation behaviour of highly porous pure titanium structures

A FIRST STEP TOWARDS THE DESIGN OF A PLASTICALLY DEFORMABLE ACETABULAR IMPLANT

By

Annemiek Groenewoud

in partial fulfilment of the requirements for the degree of

**Master of Science**

in Biomedical Engineering

at the Delft University of Technology,  
to be defended on Thursday 11 January 2018

Supervisor:	Prof. dr. ir. H. (Harrie) Weinans <sup>1,2</sup>
Daily supervisor:	K. (Koen) Willemsen, MD <sup>1</sup>
Thesis committee:	Prof. dr. ir. H. (Harrie) Weinans <sup>1,2</sup> Prof. dr. A. A. (Amir) Zadpoor <sup>2</sup> Dr. J.J. (John) van den Dobbelaar <sup>2</sup>

<sup>1</sup>Department of Orthopedics, University Medical Center Utrecht

<sup>2</sup>Department of Biomedical Engineering, Delft University of Technology

## TABLE OF CONTENT

ABSTRACT.....	5
NOMENCLATURE.....	6
1. INTRODUCTION.....	7
1.1. Project background.....	8
1.2. Aim of this study.....	9
2. ANALYTICAL BENDING PROPERTIES OF THE DIAMOND UNIT CELL.....	11
3. EXPERIMENTS.....	13
3.1. Test 1: Uniaxial compression test with cylindrical samples.....	13
3.2. Test 2: Push-in and pull-out tests – Deformation to shape and into holes.....	19
3.3. Test 3: Push-in test – Deformation process.....	30
4. DISCUSSION.....	35
5. CONCLUSION.....	37
6. REFERENCES.....	38
APPENDIX A: Test 2 - Figures of push-in test per structure.....	40
APPENDIX B: Test 2 - Micro-CT images of all samples.....	41
APPENDIX C: Test 2 - Figures of pull-out test.....	45
APPENDIX D: Test 3 - Micro-CT images of all samples.....	47

## ABSTRACT

Massive acetabular bone defects are difficult to treat with the currently available implants. Advances in additive manufacturing create new design possibilities, which allow the production of patient specific implants. These endless possibilities will enable to tune the mechanical properties of porous implants and to distribute the loads in such a way that it mimics the natural load distribution. This technique will therefore be used in the design of a new type of implant, which is a deformable acetabular implant that will fully fit in a massive acetabular defect after plastic deformation. In this way, all remaining bone will be loaded, and the physiological load distribution will be restored to maximally reduce stress shielding and to prevent further loss of bone stock. To design this new implant, more information is required on the mechanical properties of the titanium porous structures. Therefore, the aim of this study is to examine the mechanical properties and deformation behaviour of highly porous pure titanium (grade 1) structures.

The diamond unit cell was used to design three types of structures with different porosities ( $> 95\%$ ). A static compression test was performed on cylindrical samples. In addition, push-in and pull-out tests were performed on hemispherical shaped samples. The samples were compressed into specially designed moulds, which represent the acetabulum with defects, to test how these structures deform according to their surrounding shape. Micro-CT images were made during and after the test to analyse the deformation.

The cylindrical samples continuously deformed during compression and large plastic strains were measured ( $> 57\%$ ). The hemispherical samples deformed conform the surrounding mould and even penetrated into the holes. The push-in and pull-out forces are positively correlated, and these forces are lower for more porous structures. The micro-CT scans show that all unit cells within the structure do not equally deform under compression, but show a gradual, layer-by-layer deformation.

This study is a first step towards the design of a deformable implant. The results are quite promising and can function as a basis for future work.

## NOMENCLATURE

### Abbreviations

ANA	Analytical
AM	Additive Manufacturing
CP	Commercially Pure
CTAC	Custom Triflanged Acetabular Components
CT	Computed Tomography
EBM	Electron Beam Melting
EXP	Experimental
FDM	Fused Deposition Modeling
Fig.	Figure
FOV	Field of View
ISO	International Organization for Standardization
Max.	Maximum
PLA	Polylactic Acid
Prosperos	Printing PERSONalized Orthopaedic implants
PVC	Polyvinyl Chloride
SLM	Selective Laser Melting
Struct.	Structure
Ta	Tantalum
THA	Total Hip Arthroplasty
Ti	Titanium
Ti-6Al-4V	Titanium alloy with 6% Aluminium and 4% Vanadium
UMC	University Medical Center
vs.	versus
2D	Two-Dimensional
3D	Three-Dimensional

### Symbols

$a$	Length of unit cell	$\epsilon$	Strain
$E$	Elastic modulus of bulk material	$\epsilon_{EL}$	Elastic strain
$E_{ST}$	Elastic modulus of structure	$\epsilon_{PLE}$	Plateau and strain
$F$	Force on strut	$\mu$	Micro
$P$	Force on unit cell	$\rho$	Apparent density of unit cell
$d$	Diameter of strut	$\sigma$	Stress
$D$	Displacement of strut	$\sigma_S$	Yield stress of bulk material
$D_V$	Vertical displacement of strut	$\sigma_{PL}$	Plateau stress
$I$	Area moment of inertia	$\sigma_{PLE}$	Plateau end stress
$L$	Length of strut	$\theta$	Angle between strut and horizon

## 1. INTRODUCTION

The management of acetabular bone defects remains a challenging aspect of revision total hip arthroplasty (THA). There are different types of acetabular bone defects, varying in size and location [1], and it can be complicated by pelvic discontinuity, which is the separation of the ilium from the pubis and ischium [1-3].

There are multiple techniques to reconstruct acetabular bone defects, including but not limited to acetabular reconstruction rings [4, 5] or cages [6, 7], uncemented hemispherical acetabular components with [8-10] or without [11, 12] metal augments, massive structural allografts [13, 14], and impaction bone grafting [15, 16]. Which treatment technique is chosen depends among others on the type and amount of bone loss [17, 18], the quality of the bone stock [20], the presence of pelvic discontinuity and intact acetabular columns [17], the ability to achieve fixation [17] with a rigid and stable implant that allows for osseointegration [18], and the long-term predictable implant survival [18].

A relatively new treatment option for severe acetabular bone defects and pelvic discontinuity is the use of custom-made acetabular implants. These patient specific implants are designed from CT images and used for patients with massive bone defects, classified as Paprosky [19] type 3A or 3B, or as AAOS [20] type III or IV. The design of these implants depends on the acetabular bone defect. Most commonly used custom acetabular implants are custom triflanged acetabular components (CTAC). These are cages with an acetabular cup and three flanges (Fig. 1) that provide additional fixation on the ilium, ischium, and pubis [18, 21, 22].



*Fig. 1 Example of a custom triflanged acetabular implant [23].*

The main advantages of the customized technique are the precise fit in the defect [18, 22, 24] and the initial stability of the implant [18, 21, 25]. The flanges contribute to the stability of the implant, but it also results in a drawback related to the load distribution. The bone to which the flanges are attached, probably carries more of the external loads than the surrounding bone, in particular in the deep layers. The external load is therefore unequally distributed and transferred in an un-physiological way. This may result in stress shielding and bone resorption of the surrounding bone in the deep layers of the acetabulum. Another disadvantage is that it is a complex and time-consuming design and manufacturing process [17, 18, 21, 26]. However, this is improving by the upcoming 3D metal printing technique.

The metal printing technique is increasingly better, faster, and less expensive. Nowadays, it is already possible to produce custom metal implants and with the continuously improving technology it becomes even more attractive to produce this type of implants. One of the improvements is related to porous structures. The 3D printing technique enables the production of fully porous implants. Porous structures are currently used to facilitate bone ingrowth, but may also be used to tune the implant's mechanical properties. The natural distribution of the external load can therefore be mimicked, which would maximally reduce stress shielding and prevent further loss of bone stock.

To avoid stress shielding, the loading of the bone surrounding the implant should be as natural as possible, meaning it should resemble the healthy anatomical situation [21, 27]. There are two main design variables to play with in order to achieve an optimal load distribution: the design (1) and the mechanical properties (2) of the implant. A full fit of the implant in the acetabular defect can ensure that all remaining bone is loaded, and a more equal load distribution is achieved. To prevent resorption, this should ideally be done without the use of flanges to avoid any stress concentration. In addition, the mechanical properties of the implant can be tuned since it is possible to produce highly porous structures. This offers the opportunity to reduce the stiffness of the implant, while maintaining the required strength.

## 1.1. Project background

The graduation project is embedded in a main project that aims to design an acetabular implant with a deformable part that will fully fit in a massive acetabular defect after plastic deformation. The porous, 3D printed, acetabular implant should be deformed during the operation resulting in a perfect fit and initial stability of the implant in the massive acetabular defect.

The advantages of a fully fit of the implant in the defect will be that all the remaining acetabular bone is loaded and that there is no concentrated load along the ridges of the acetabulum. The load will therefore be more equally distributed across the host bone, resulting in a more physiological load distribution compared to the currently used custom made acetabular implants with flanges. This will not only prevent bone resorption, but due to the perfect fit there will also be a large bone-implant interface area at which bone growth can take place to increase the implant's fixation and stability.

These goals may be achieved by playing with the design and the mechanical properties of the implant. To design a new implant, several requirements, constraints, and challenges should be considered. Some of them are listed below.

### *Mechanical*

- The mechanical properties of the implant should match the mechanical properties of the host bone to redistribute loads and to avoid stress shielding.
- The implant should meet the required mechanical properties, both before and after the plastic deformation, to prevent mechanical failure.
- The implant should not further deform after the implantation. The implant should therefore be maximally deformed during the operation or further deformation should be prevented after implantation.
- It should not be considered a bad thing if struts inside the porous structure break during the deformation process, as long as each strut is still connected to at least one other strut (1), and no metal particles are released (2). This is important, since metal debris can cause inflammatory responses of the host, which may result in osteoclast stimulation and aseptic loosening [28].

### *Implantation*

- The maximal forces the surgeon can apply to deform the implant should be considered in the design of the implant.
- The host bone should not break during or after the operation. Therefore, the various mechanical properties of the patient's acetabulum (thickness, quality, porosity, etc.) should be considered during the design and implantation of the implant.
- It must be possible to fixate a polyethylene liner in the metal porous structure.
- It must be possible to implant the deformable cup in the correct position and orientation after the plastic deformation.
- The implant should not dislocate or rotate after the implantation, so there should be initial stability.

### *Biocompatibility*

- To facilitate bone ingrowth, the porosity should be above 50%, and the pore size should be between 50 and 800  $\mu\text{m}$  [29]. The implant should also comply with these bone ingrowth requirements after the deformation.
- The structure should be highly porous with interconnecting pores to facilitate the transport of nutrients and metabolic waste products [30].
- The structure should enable cells to attach, proliferate, and differentiate [30].

### *Manufacturing*

- The implant should be producible with one of the metal additive manufacturing (AM) processes, for example with selective laser melting (SLM) or electron beam melting (EBM).
- The minimum strut thickness that can be produced by most of the current AM technologies is around 200  $\mu\text{m}$  [29].
- The implant should be free of loose metal powder and sterilized before implementation.

## **1.2. Aim of this study**

The main project is too large for a graduation project. Therefore, it was decided to focus on only a specific part of this project. In order to get a better feeling of the problem, a model of an acetabulum was designed (Fig. 2). The model was based on CT images of a patient with a massive bone defect who was treated at the UMC Utrecht. The CT images were segmented using Mimics software and the STL-file was printed by ProtoSpace (Utrecht, Netherlands) with a Fused Deposition Modeling (FDM) printer using the material polylactic acid (PLA).



**Fig. 2** Acetabular model printed with FDM printer.

To make an optimal implant design, more information is required on the mechanical properties, in particular on the plastic deformation of the implant design. This study therefore focuses on the mechanical properties and deformation possibilities of porous titanium structures. To be more specific, most attention will be paid to the deformation possibilities of highly porous samples printed from commercially pure (CP) titanium.

Questions that will be investigated are:

- Is there is a large plastic deformation possible with highly porous pure titanium structures?
- How does the strut length/thickness ratio influence the plastic deformation?
- Do the porous structures deform according to their surroundings under compression?
- What does the deformation process look like?
- What forces are needed to deform the structures?

To answer these questions, porous titanium samples will be designed, printed, and mechanically tested (see section 3). In addition, analytical calculations are performed and compared with the experimental results to predict the theoretical plastic deformation of diamond cellular structures with a certain unit cell size. The analytical calculations of the elastic modulus can be found in the next section.

## 2. ANALYTICAL BENDING PROPERTIES OF THE DIAMOND UNIT CELL

The elastic modulus of diamond cellular structures will be analytically calculated in this section. The diamond unit cell will be tested in the experiments and there is interest in the relation between the unit cell size and the plastic deformation for this unit cell type. Therefore, the goal is to predict the total deformation of a diamond cellular structure for a specific unit cell size.

To do this, different steps will be taken in which the analytical calculations will be combined with the experimental results. The elastic modulus of the diamond cellular structures will be analytically calculated for the three unit cell sizes that are also experimentally tested in test 1.

Fig. 3 is a schematic 2D representation of the diamond unit cell. The symbols in this figure are used in the following formulas.

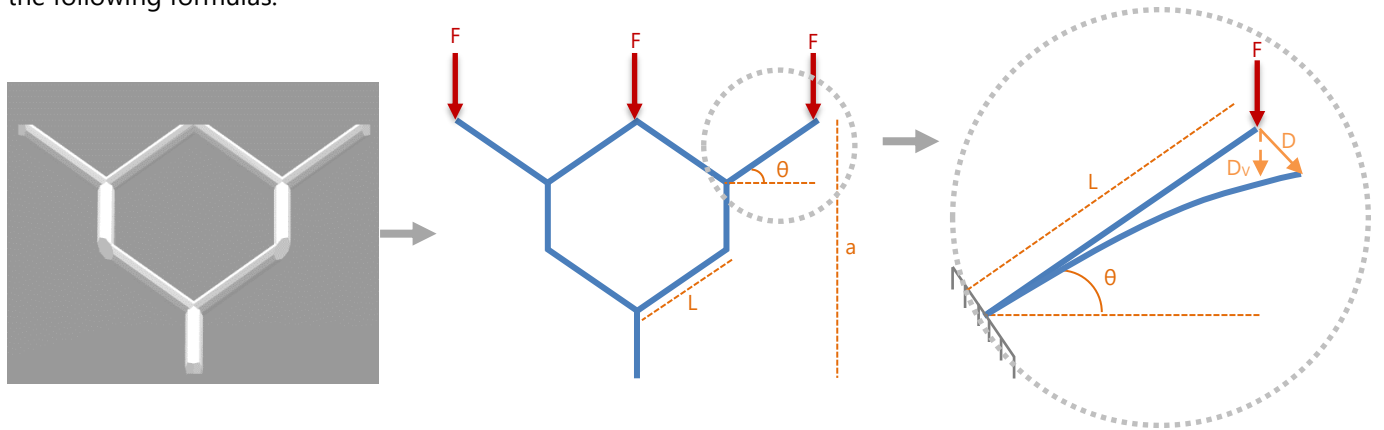


**Fig. 3** Schematic 2D representation of a diamond unit cell (left and middle) and a strut (right).

The elastic modulus and unit cell properties that are used for the calculations are listed in Table 1. The elastic modulus of the bulk material is based on the mechanical properties of standard annealed wrought commercially pure titanium grade 1 listed in the publication of Wauthle et al. [31].

Elastic modulus of the bulk material	<b>E</b>	103 GPa
Angle between strut and horizon	<b>θ</b>	35.26° (= 35.26 · π / 108 rad)
Strut thickness	<b>d</b>	200 μm

**Table 1** Mechanical bulk properties of CP Ti grade 1 and diamond unit cell properties.

The used variables are the strut length (**L**), and the force acting on the unit cell in the vertical direction (**P**). The strut length/thickness ratios will be varied by changing the strut lengths. The strut thickness is set to 200 μm, which is the minimum thickness that can be produced by most of the current AM technologies.

The formulas that are used to calculate the apparent densities, stresses, and strains of the diamond unit cells can be found in Table 2. The formulas are obtained from the paper of Ahmadi et al. [32]. Analytical solutions were presented in that study to predict the mechanical properties of cellular structures made from diamond unit cell. The formulas in Table 2 are based on the Euler-Bernoulli beam theory. These equations showed to be quite accurate for structures with small apparent densities [32]. The maximum apparent density of the structures tested in this research is 0.073, which is small enough to use the Euler-Bernoulli beam theory as a reliable method.

Force acting on a strut in vertical direction	<b>F</b>	$F = P/4$
Apparent density, unit cell	<b><math>\rho</math></b>	$\rho = \frac{3 \cdot \pi \cdot \sqrt{3} \cdot d^2}{16 \cdot L^2}$
Second moment of inertia	<b>I</b>	$I = 1/4 \cdot \pi \cdot (d/2)^4$
Length, unit cell	<b>a</b>	$a = 2\sqrt{2} \cdot L \cdot \cos(\theta)$
Total deformation of a strut in vertical direction	<b><math>D_v</math></b>	$D_v = \frac{P \cdot L^3 \cdot (\cos(\theta))^2}{12 \cdot E_s \cdot I}$
Stress, unit cell	<b><math>\sigma</math></b>	$\sigma = \frac{P}{8 \cdot L^2 \cdot (\cos(\theta))^2}$
Strain, unit cell	<b><math>\epsilon</math></b>	$\epsilon = D_v/a$

**Table 2** Formulas to calculate the stress and strain of diamond unit cells.

The elastic modulus of the cellular structure is calculated by dividing the stress by the strain ( $E_{ST} = \sigma/\epsilon$ ). It is assumed that the stresses and strains of the unit cell are representative for a cellular structure made of several unit cells.

The theoretical strut lengths of the experimental specimens in test 1 are 0.75 mm (struct. 1), 1.18 mm (struct. 2), and 1.62 mm (struct. 3). The calculated elastic moduli of these structures are 199 MPa, 32.5 MPa, and 9.15 MPa, respectively. These three elastic moduli will be compared with the experimental results, to verify the accuracy of the analytical solutions. Subsequently, the correlation between the elastic modulus and the plastic strains of the experimental results will be estimated. Based on that, the strain of a specific unit cell size could be predicted using the analytical formulas and the estimated correlation between the elastic modulus and the plastic strain. This can be found in the discussion of test 1.

### 3. EXPERIMENTS

To evaluate the mechanical properties of porous 3D printed structures, several mechanical tests were performed and evaluated with the help of mechanical testing machines and a micro-CT scanner. The materials and methods, results, discussion, and conclusions are reported per test. The overall discussion and conclusion can be found in sections 4 and 5.

#### 3.1. Test 1: Uniaxial compression test with cylindrical samples

The static compressive properties of highly porous pure titanium structures were investigated in this test (Fig. 4). The plastic deformation properties of the samples were of main interest.

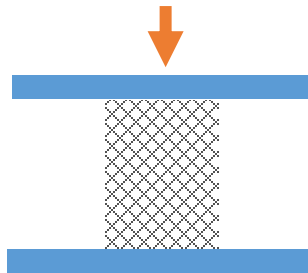


*Fig. 4 Schematic representation of test 1.*

##### 3.1.1. Materials and methods

Porous cylindrical samples with a height of 20 mm and a diameter of 15 mm were produced by 3D Systems (Leuven, Belgium) with a SLM machine. The samples were made from commercially pure (CP) titanium grade 1 and tested as manufactured, so no heat treatment was applied. The unit cell type of these porous structures was diamond (Fig. 5). Three different porosities were designed in 3DXpert software (3D Systems) by changing the strut length of the unit cells. The strut diameter was kept constant (200  $\mu\text{m}$ ). Table 3 shows the designed properties of the porous samples. Samples of the three structures have been depicted in Fig. 6. Three samples were printed per structure, resulting in nine cylindrical samples to be tested in total.

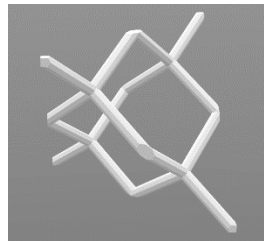


*Fig. 5 Diamond unit cell type.*

	Unit cell size (X,Y,Z) [mm]	Strut length [mm]	Strut and node diameter [mm]	Strut length/thickness ratio	Theoretical density [%]	Theoretical porosity [%]
<b>Struct. 1</b>	2, 2, 2	0.75	0.2	3.75	4.4	95.6
<b>Struct. 2</b>	3, 3, 3	1.18	0.2	5.9	2.0	98.0
<b>Struct. 3</b>	4, 4, 4	1.62	0.2	8.1	1.2	98.8

*Table 3 Designed characteristics of the porous structures in test 1.*

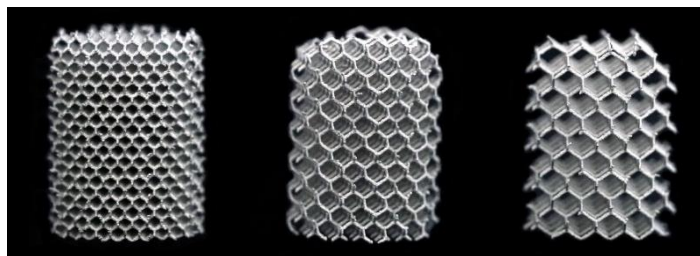


**Fig. 6** Cylindrical samples in test 1. From left to right: structure 1, 2, and 3.

The static mechanical test was carried out in accordance with the standard ISO 13314 [33]. A Lloyd LR5KPlus Universal Materials Testing Machine was used with a 5 kN load cell and compression plates. The samples were compressed with a constant deformation speed of 2.4 mm/min till a load of 4.90 kN was reached.

The initial dimensions of the samples (length and diameter) were measured before the start of the test and entered in the software. A sample was placed between and in the middle of the platens of the test machine. During the test, the load and displacement data were recorded. The sample was removed after the end of the test and the next sample was positioned. This was repeated till all cylindrical samples were tested.

### 3.1.2. Results

The results of the static compression test can be found in Fig. 7. The red, blue, and green lines represent samples of type 1, 2, and 3 respectively. The three lines per colour represent the three samples, which hardly show any differences.

All structures show ductile material behaviour and the structures continuously deformed during compression, especially structures 2 and 3. Large strains were measured (up to at least 57%) at relatively low stresses (max. 10 MPa, related to structure 1). The higher the porosity of the structure, the lower the yield and plateau stress, and the higher the strain.

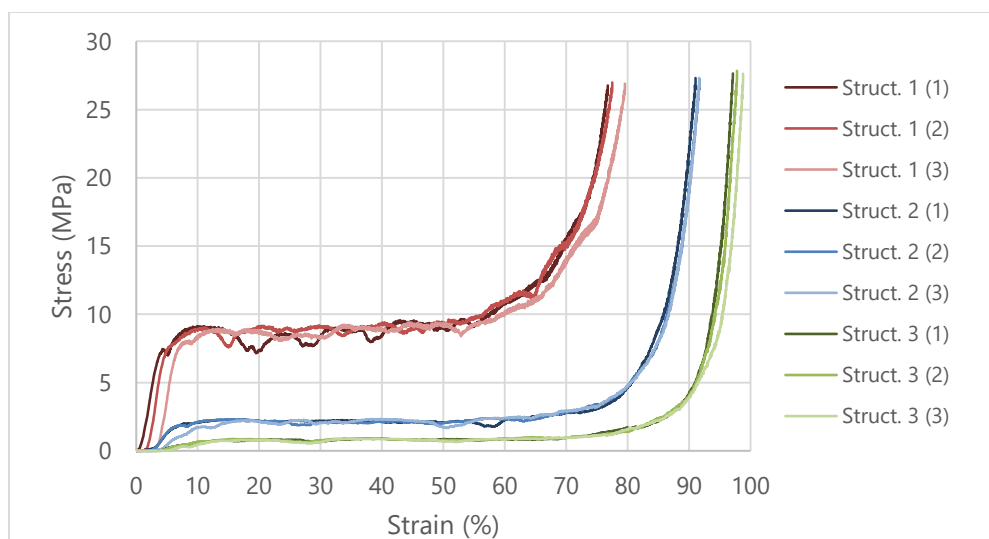


**Fig. 7** Stress-strain curves of the cylindrical samples in test 1.

### 3.1.3. Discussion

The samples are not heat treated, because the samples have thin struts (200  $\mu\text{m}$ ) and it was assumed that a heat treatment has negligible effect on the mechanical properties of such thin struts. However, this assumption has not been tested, so it is unclear if this assumption is correct. Heat treatments are often applied to titanium implants and the final implant will likely also be heat treated. It is known that a heat treatment can change the mechanical properties, especially for more dense parts. It is often applied to

reduce residual stresses in bulky parts [31], and it generally increases the ductility of the material. The final implant will not only contain very thin struts, but it will also consist of thicker struts and less-porous regions. It is therefore assumed that the heat treatment will have a larger effect on the final implant compared to the samples of this test.

To investigate the possibility of large plastic deformations with porous titanium structures, the decision was made to evaluate just one unit cell type using various porosities. This was decided to limit the number of variables, while the unit cell type will also have a smaller effect on the deformation than the porosity. The porosity was therefore varied by changing the strut length.

Pure titanium was used, since this material is highly ductile. This was shown in the research of Wauthle et al. [31], in which the mechanical properties of pure titanium were compared with tantalum (Ta) and Ti-6Al-4V ELI. Ta showed excellent in vivo performance, but the disadvantage is that it is very expensive. However, Wauthle et al. [31] concluded that porous pure titanium structures exhibited comparable mechanical properties. Compared to Ti-6Al-4V ELI, pure titanium is more ductile. Since the aim is to design a deformable implant, a highly ductile material is needed. The yield strength of pure titanium is about half of Ti-6Al-4V ELI, and it has a comparable stiffness [31]. Another advantage of pure titanium is that it contains no potential hazardous or toxic elements like aluminium or vanadium [31], so pure titanium seemed to be the most suitable material for the implant.

The diamond unit cell was chosen because it has a relatively low stiffness, and it is relatively easy to print using AM techniques [32]. Ahmadi et al. [34] investigated the mechanical properties of six different unit cells and found that the unit cells could generally be divided in two groups (stiff and compliant) with the diamond and rhombic dodecahedron unit cells in the lower stiffness group. Since a highly deformable structure is needed, a lower stiffness structure is preferred. The diamond unit cell was preferred over the rhombic dodecahedron unit cell by 3D systems, because diamond structures are relatively easy to print.

Despite these considerations, there might be another, more suitable, unit cell. More research will therefore be needed to find the most optimal unit cell type. The relatively simple structure is an advantage for printing, but the disadvantage is that the struts from one unit cell only provide limited support to each other. The entire diamond unit cell can therefore easily collapse when one of the struts fails. [34] This does not necessarily have to be a problem, as long as it provides the required mechanical strength, and all struts are still connected at one of its ends.

It was decided to print samples with large strut length/thickness ratios, to achieve relatively large deformations. The rationale for this was that it should be easier for large and thin struts to bend (lower bending stiffness). This is comparable to a netting that has an extremely large stick length/thickness ratio. The relative thin struts have lower bending stiffness.

For this research, unit cell sizes 2x2x2, 3x3x3, and 4x4x4 mm were chosen. In this way, three completely different strut length/thickness ratios were examined. Smaller (1.5x1.5x1.5 mm) and larger (5x5x5 mm) unit cell sizes were also considered, but the 1.5 mm size seemed too dense and the 5 mm size seemed quite fragile in the design software. A unit cell size of 1.5x1.5x1.5 mm is the standard size that is normally used for implants that are not supposed to deform, so it was clear that a larger unit cell size had to be tested in this research.

The pure titanium samples show typical stress-strain curves for porous structures under compression, which can be divided into three main regions. The first region is the initial linear elastic region (1), followed by a relatively long plateau region (2). In this region, plastic deformation takes place. There are only small fluctuations in stress shown, especially for the more porous structures 2 and 3. The last region is the densification region (3), in which the stress exponentially increases. This densification stage started at strains of about 63%, 69%, and 72%, for structures 1, 2, and 3 respectively. In this region, stiffening of the porous structures takes place [34], which is a typical behaviour for large strains after the plateau region [32].

The higher the porosity of the structure, the larger the plateau region. The strut length/thickness ratio therefore clearly influences the plastic behaviour of the structure as a whole.

*Prediction of bending properties:*

As mentioned in section 2, the experimental results should be compared with the analytically calculated elastic modulus. Furthermore, the correlation between the elastic modulus and the total deformation will be estimated.

The analytically calculated elastic moduli have been plotted in Fig. 8, next to the experimentally obtained results. The slopes of the calculated lines are quite comparable to the slopes of the linear elastic regions of the corresponding structures. The analytical method therefore seems to be quite accurate.

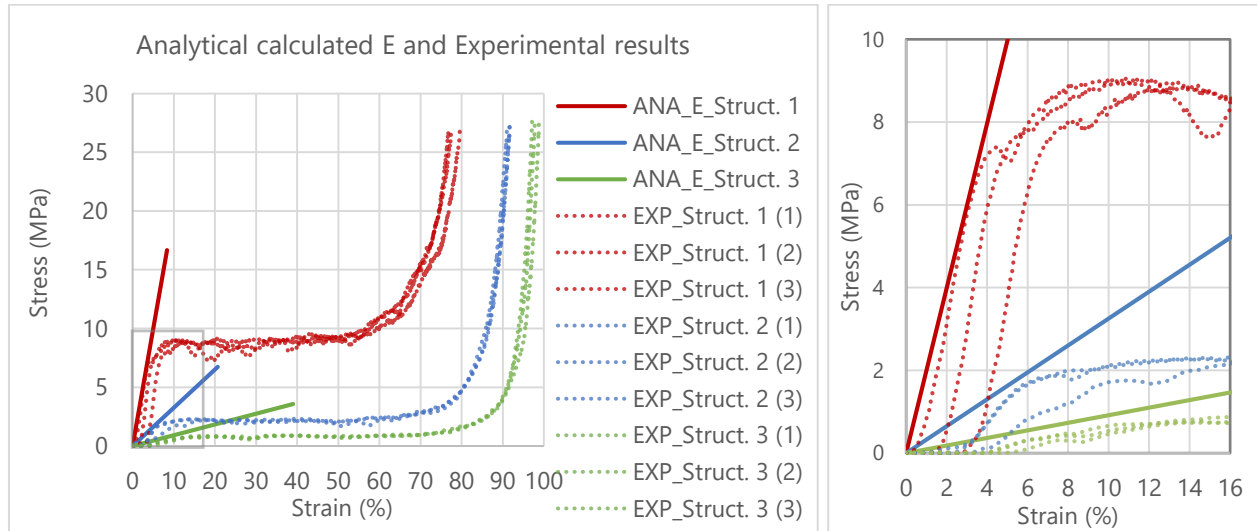


**Fig. 8** Analytically calculated elastic modulus of the three tested structures and the experimental results.

Only the linear elastic region of the structures is calculated with the formulas. However, to say something about the total deformation of the structure, a link should be found between the elastic and the plastic deformations. Therefore, the elastic strain and the plastic strain at the end of the plateau region should be compared. To do so, the average plateau stresses and the plateau end stresses of the three tested samples are calculated. The plateau stresses are calculated by measuring the average stresses between 20% and 40% strain, and the plateau end stresses are calculated by multiplying the plateau end stresses by 1.3 (in accordance with the standard ISO 133314 [33]). These plateau (end) stresses are shown in Fig. 9.

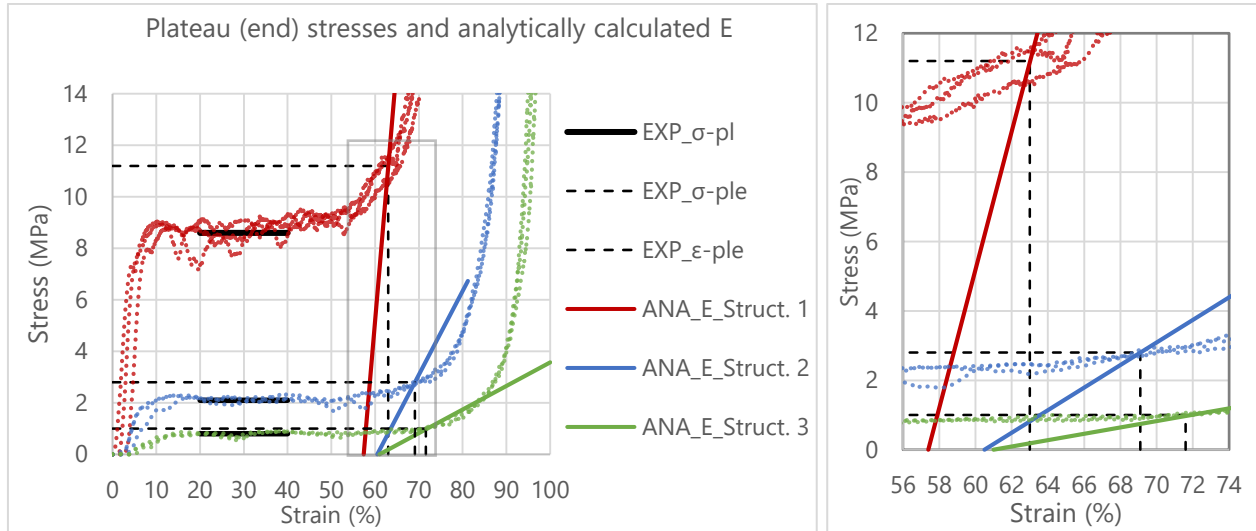


**Fig. 9** Elastic and plastic stain at the plateau end of the three tested structures. Based on the average plateau stresses and the analytically calculated elastic modulus.

The elastic strain is subtracted from the plateau end stress to obtain the plastic deformation at the end of the plateau region. Therefore, the calculated elastic moduli are shifted to the right till the lines intersect the plateau end on the curves. Fig. 9 clearly shows that the elastic strain increases if the elastic modulus decreases. The differences between the plastic strains at the end of the plateau region are therefore quite small for the three structures, especially between structure 2 and 3.

The structure can theoretically also be compressed further in the densification region, but the stresses rapidly increase in that region. To investigate the maximum achievable deformation, the strains at the end of the densification region are also calculated. To do this, the elastic strain is subtracted from the strain at the end of the densification region. All strains are listed in Table 4.

	Elastic modulus	Elastic strain (= $\epsilon_{EL}$ )	Plastic strain at end of plateau region (= $\epsilon_{PLE} - \epsilon_{EL}$ )	Strain at end of densification region minus elastic strain (= $\epsilon_{LIMIT} - \epsilon_{EL}$ )
<b>Struct. 1</b>	199 MPa	5.6 %	57.4 %	72.3 %
<b>Struct. 2</b>	32.5 MPa	8.6 %	60.5 %	82.9 %
<b>Struct. 3</b>	9.15 MPa	10.6 %	61.0 %	89.3 %

**Table 4** Elastic strain, strain at end of plateau region, and strain at limit.

The last step is to correlate the elastic modulus of the cellular diamond structure with the plastic strain. This will enable the prediction of the plastic strain of a structure, based on the elastic modulus of its specific unit cell size. The elastic moduli are plotted against the strains at the end of the plateau region and against the strain at the end of the densification region in Fig. 9 and Fig. 11, respectively.

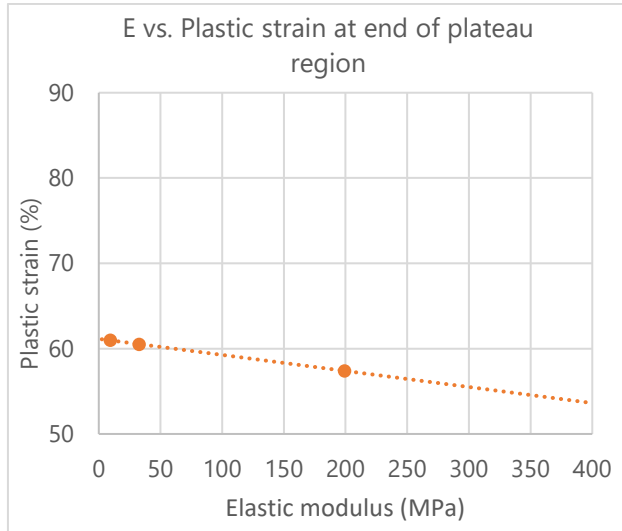


**Fig. 10** Elastic modulus of cellular structures versus the plastic strain at the end of plateau region.

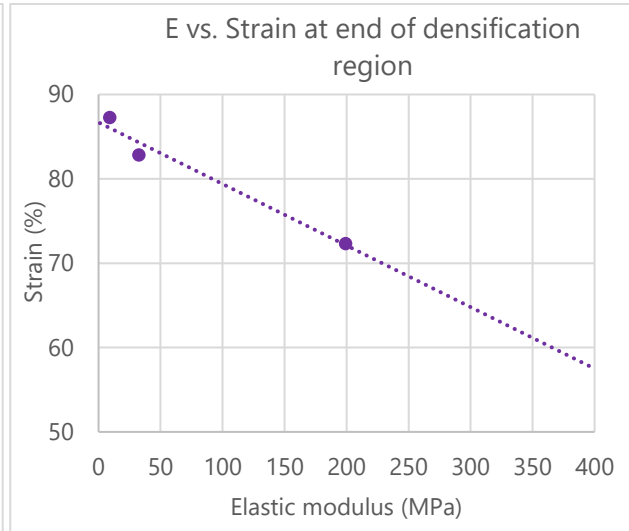


**Fig. 11** Elastic modulus of cellular structures versus the strain at limit minus the elastic strain.

Linear trendlines are drawn in Fig. 10 and Fig. 11. Three points are not enough for an accurate trendline, but the line fits quite well with the points in Fig. 10. The trendline in Fig. 11 is less accurate, since it is drawn below the left point. However, the figures clearly show that the elastic modulus is negatively correlated with the strain. With a decreasing elastic modulus, there is a larger increase in strain at the end of the densification region compared to the increase in strain at the end of the plateau region. The influence of the strut length on the plastic deformation will therefore slightly increase when the structure is deformed up to the end of the densification region. The theoretical maximum strain at the end of the densification region will probably be about 90%, based on the results of the three tested structures (see Fig. 11). Fig. 9 shows that, theoretically, a maximum plastic deformation of 61.2% can be achieved, when the structure is deformed up to the end of the plateau region.

Fig. 9 and Fig. 1 show that there are almost no higher plastic deformations possible for structures with a larger strut length than structures 2 and 3 (1.18 and 1.62 mm respectively). The measured plastic deformation at the plateau end for structure 3 is about 61%, and a maximum theoretically achievable plastic deformation is 61.2% when deformed up to the plateau end. This is because the elastic modulus decreases when the strut length increases, resulting in a larger elastic strain. It would therefore be almost impossible to increase the plastic strain for unit cell sizes that are larger than those tested in this study.

The formulas in section 3 and the aforementioned correlation can be used to predict the plastic deformation of diamond unit cells with various strut length/thickness ratios.

### 3.1.4. Conclusion

A static compression test was performed on nine highly porous (> 95%) cylindrical samples made from pure titanium. The results are quite promising, because there were large plastic deformations measured, up to at least 57%, while the maximum compressive stresses were 10 MPa. These plastic deformations are desirable for (the outside layer of) the final implant.

### 3.2. Test 2: Push-in and pull-out tests – Deformation to shape and into holes

This test examines the extent to which the porous samples deform according to the surrounding shape and penetrate into the holes. The surrounding shape will be a mould, which represents the acetabulum (Fig. 2). Therefore, two tests were performed, and micro-CT scans were made after the first test to analyse the samples (see Fig. 12). First, a push-in test was performed. Porous samples were compressed in moulds with holes to check how the samples deformed to the shape of the mould and penetrated into the holes. Secondly, micro-CT scans were made from the samples in the moulds to analyse the structures and deformations after the compression test. Finally, the samples were pulled out the moulds. The pull-out forces were measured to get an idea of the fixation and initial stability of the samples.

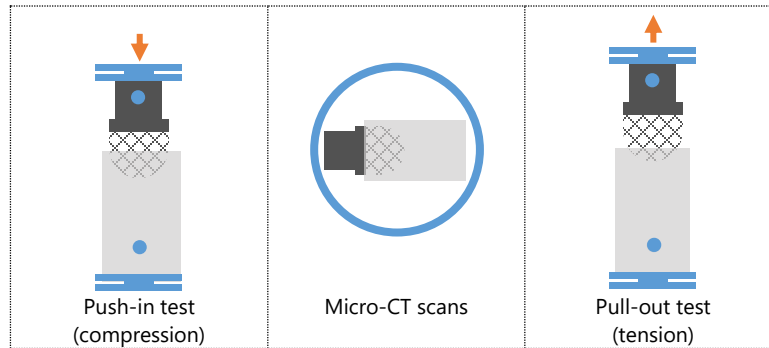


Fig. 12 Schematic representation of test 2.

#### 3.2.1. Materials and methods

Again, all samples (Fig. 13) were produced by 3D Systems (Leuven, Belgium) with an SLM machine. The samples were made from CP titanium grade 1 and tested as manufactured, so no heat treatment was applied. Porous hemispherical samples with non-porous fixture parts were printed in two different sizes (Fig. 14) and in three different structures (equal to the structures from test 1, see Table 3). Three samples were printed per type, resulting in eighteen samples to be tested in total. One sample (with structure 1 and size 1) was used for a trial test, so only the results of seventeen samples were reported.

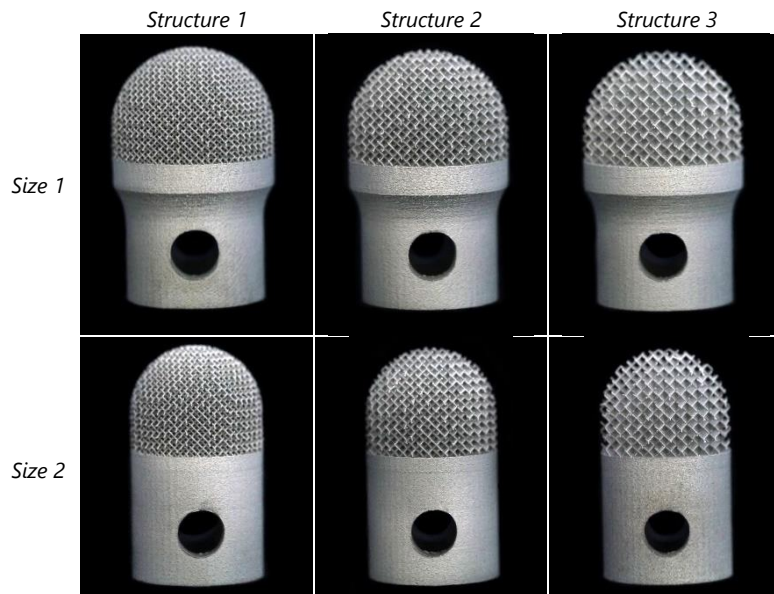
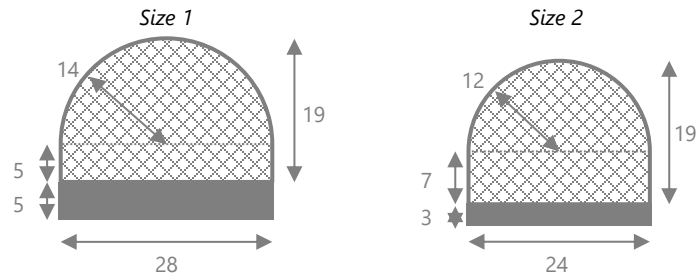
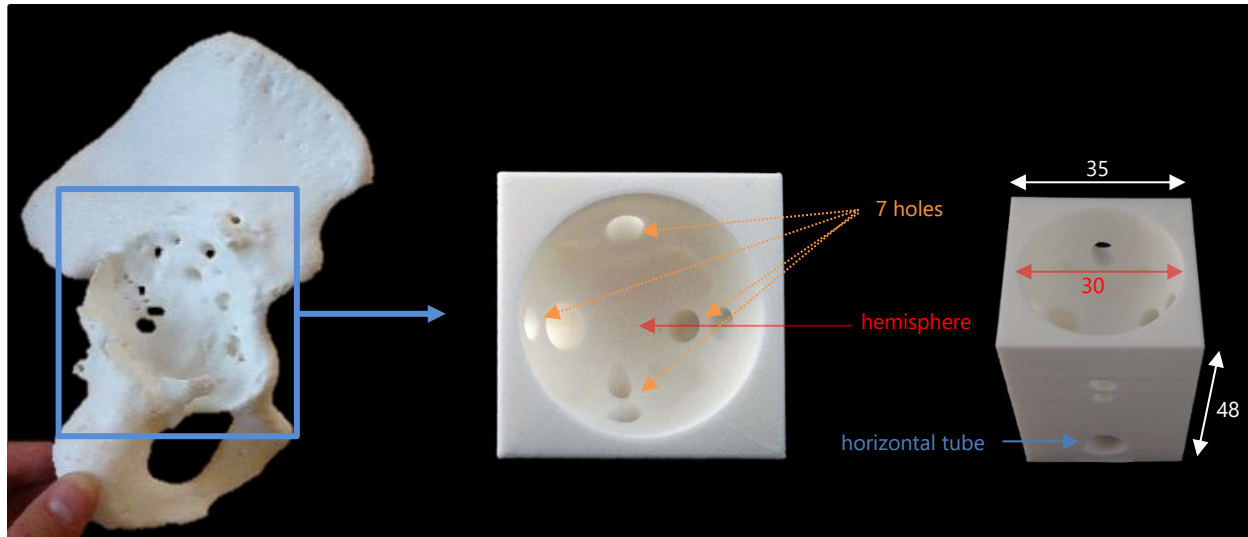


Fig. 13 The six different sample types that are tested in test 2.



**Fig. 14** Dimensions (mm) of samples test 2.

The design of the moulds was based on the acetabular model (Fig. 2) and made using SolidWorks 2017 software and Geomagic Freeform Plus software. The moulds consisted of a hemisphere, with several deformations and holes protruding to the outside of the mould. This represents an acetabulum with a massive defect, screw holes, and slight deformations (Fig. 15). There were also two tubes (horizontal and vertical) in the lower part of the mould that were used to connect the mould to the testing machine.



**Fig. 15** From acetabular model to mould. Middle and right: mould with its holes/tubes and dimensions.

The titanium samples were undersized with respect to the size of the hemisphere, as shown in Fig. 16. This will also be the case for the deformable part of the implant, which will be slightly smaller than the defect to enable its deformation. The samples from size 1 were less undersized compared to the samples from size 2.

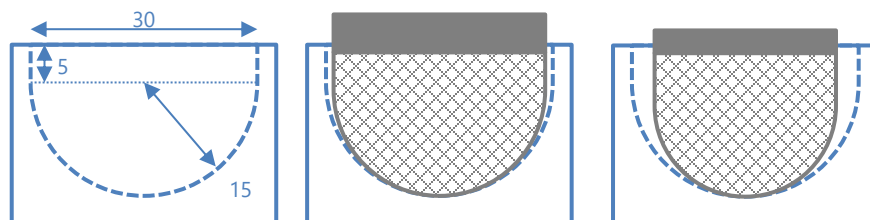


**Fig. 16** Size of hemisphere in mould (left) with respect to samples size 1 (middle) and size 2 (right).

Seventeen moulds were printed in total for this test with the Ultimaker 2+ from PLA with 50% infill.

#### *Push-in test:*

The compression test was performed with a 5 kN Lloyd LR5KPlus Universal Materials Testing Machine, or, when more loading was required to deform the sample, with a Zwick 1455 universal testing machine that could load up to 20 kN. The test set-up is shown in Fig. 17. The adapter was connected to the load cell, which was connected to the testing machine. The mould was placed on the anchor pin and connected with a pin in his term. The sample was place in between the adapter and the mould. The crosshead was moved down till the sample reached the mould and the lower collar was turned till it touched the sample. This was the starting position of the test.

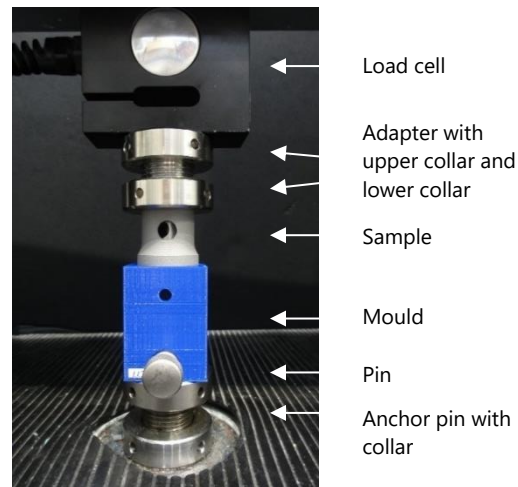


**Fig. 17** Set-up before the start of the push-in test and definitions of components.

A constant deformation speed of 2.4 mm/min was applied to the sample up to a displacement of 8.5 mm. The machine software recorded the applied load and the extension over time. After the 8.5 mm displacement, the sample-mould combination was removed from the machine and replaced by the next combination. These steps were repeated till all samples were examined.

#### *Micro-CT scans:*

The micro-CT scans were performed on a Caliper LifeSciences Quantum FX micro-CT scanner with 90 kV and 200  $\mu$ A. The samples were scanned for 180 seconds with a field of view (FOV) of 30 mm, resulting in a resolution of 16.9492 pixels/mm and a voxel size of 59  $\mu$ m<sup>3</sup>.

Per scan, one sample-mould combination was placed on its side into a tube that was partially surrounded with a copper layer (Fig. 18). This layer functions as a filter that creates a more uniform radiation that passes through the object. This will improve the quality of the scan. After the scan was made, the sample-mould combination was removed and replaced by the next. This was repeated till all samples were scanned.

The software ImageJ was used in combination with the 3D plugin to analyse the structures and to make images. In addition, the software program RadiAnt DICOM viewer was used to make multiplanar (front, side, and top) images of the deformed samples inside the moulds.

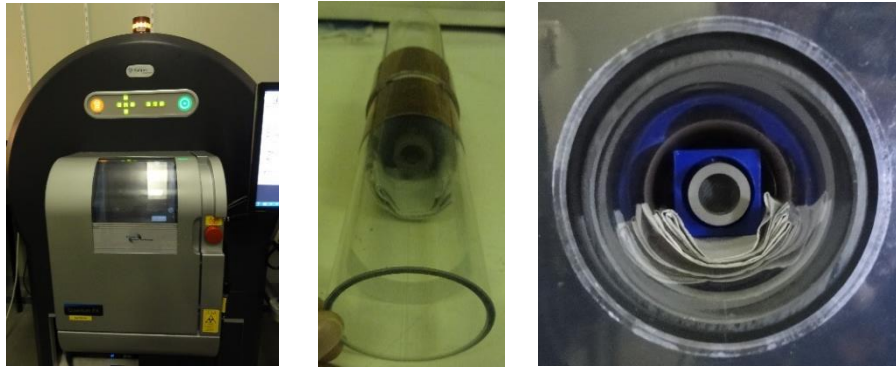


**Fig. 18** Left: micro-CT scanner. Middle: sample-mould combination in tube with copper layer. Right: tube in scanner.

#### *Pull-out test:*

The pull-out test was performed with the Lloyd LR5KPlus mechanical testing machine that was also used for the push-in test. The test set-up is shown in Fig. 19. A 5 kN load cell was connected to the testing machine, and the adapter was connected to the load cell and fixated with the upper collar. The mould was placed on the anchor pin and connected with a pin. The crosshead was lowered till the adapter was positioned inside the sample. The sample was fixated to the adapter with a second pin and both remaining collars were turned till they touched the sample/mould. This was the starting position of the test.

The pull-out speed was equal to the push-in speed (2.4 mm/min). The test was continued up to a displacement of 10 mm, so the entire sample was removed from the mould. The machine software recorded the tension forces and the extension over time. After the test was finished, the sample-mould combination was removed and replaced by the next combination till all samples were tested. Unfortunately, one sample with structure 3 (size 2) was accidentally released from the mould after the push-in test, so no pull-out test was performed on this sample.



**Fig. 19** Set-up before the start of pull-out test.

### **3.2.2. Results**

#### *Push-in test:*

All samples are deformed and fixed in the mould after the push-in test. Fig. 20 shows some of the samples that are compressed into the moulds. There is some penetration of the structures into the holes visible, especially in the lower holes that are closer to the bottom of the mould (Fig. 21).

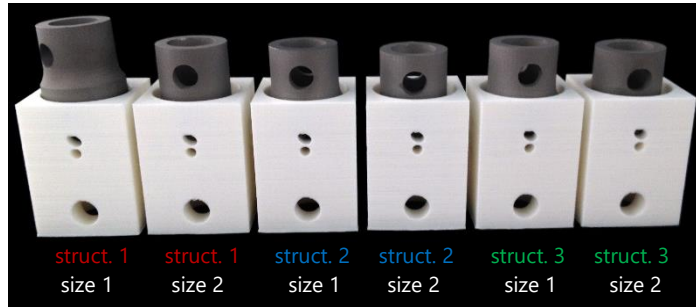


**Fig. 20** Samples compressed in the moulds after the push-in test.



**Fig. 21** Relatively high and low positions of the holes in the mould.

Fig. 22 shows the extension-load curves of all samples from the push-in test. The red, blue, and green lines represent the samples with structure 1, 2, and 3, respectively. The solid and dotted lines represent the samples from size 1 and 2, respectively. The test results with a 'Z' in the legend refer to the samples that are (partially) tested with the 20 kN Zwick testing machine. Figures of the push-in test results per structure can be found in appendix A.

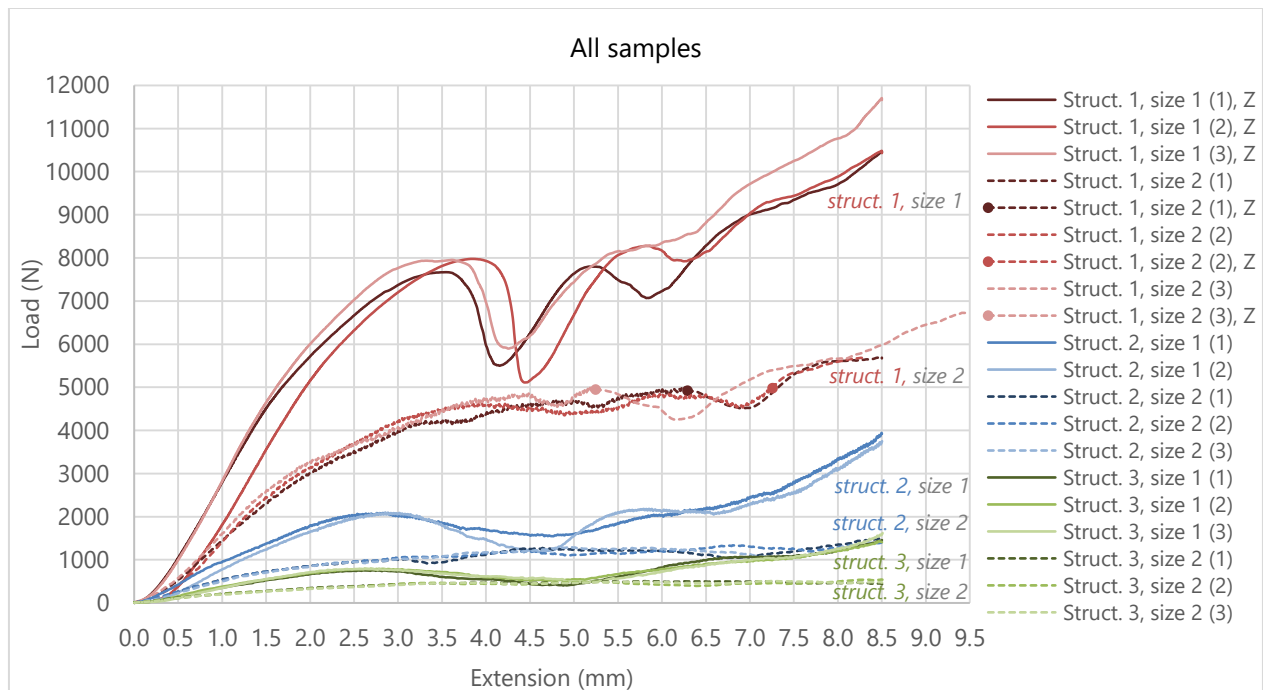


**Fig. 22** Push-in test: extension vs. load of all samples in test 2.

There is almost no difference between the samples from the same type (same structure and size), so the data per type is consistent. There are differences between the sample structures and sizes. The push-in loads are the highest for all samples with structure 1 and the lowest for all samples with structure 3. The loads for the samples with structure 1 are at least three times as high as the loads of structure 2 and 3.

The push-in loads of samples in size 1 are higher compared to the loads of samples in size 2, looking at the same structures. For example, the loads for 'structure 2-size 1' are higher than the loads for 'structure 2-size 2', but lower than the loads for 'structure 1-size 1'. Another difference is that loads for samples in size 1 fluctuates more than the load used for samples in size 2. The load needed for size 2 is more constant over the extension range.

*Micro-CT scans:*

This section contains 3D visualizations of the deformed samples. There are only small differences between the samples per type (with the same structure and size), so Fig. 23, Fig. 24, and Fig. 25 only show the images of one sample per type. The remaining images of all samples can be found in Appendix B.

Fig. 23 and Fig. 24 show the top and side view of the deformed samples, respectively. The grey dotted lines in Fig. 24 indicate the initial, undeformed shape of the porous part of the samples. So, the area between the dotted line and the sample is the deformed area. Multiplanar images of the deformed samples inside the moulds can be found in Fig. 25, which clearly shows the porous structures in some of the holes.

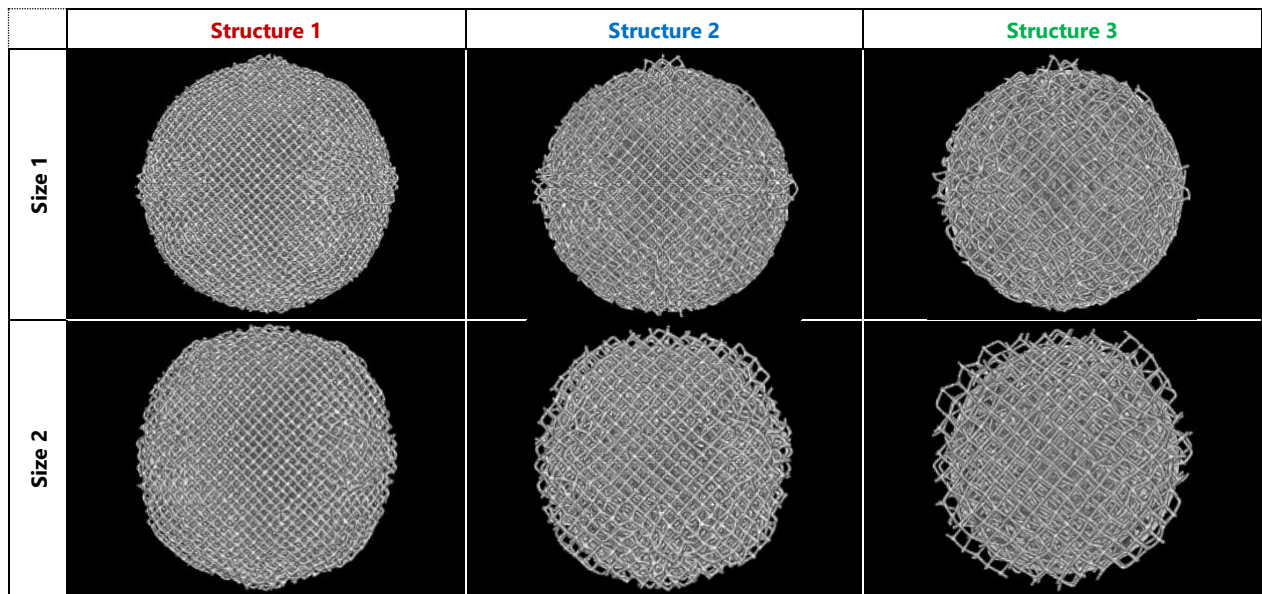


*Fig. 23 Images of deformed samples in test 2, top view.*

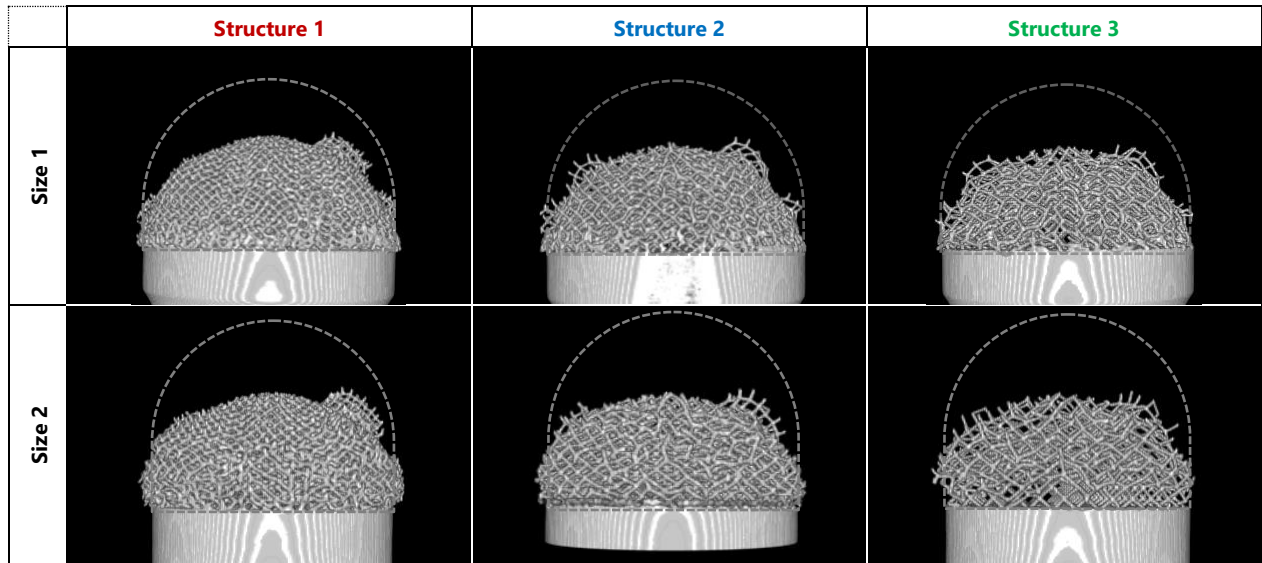


*Fig. 24 Images of deformed samples in test 2, side view.*

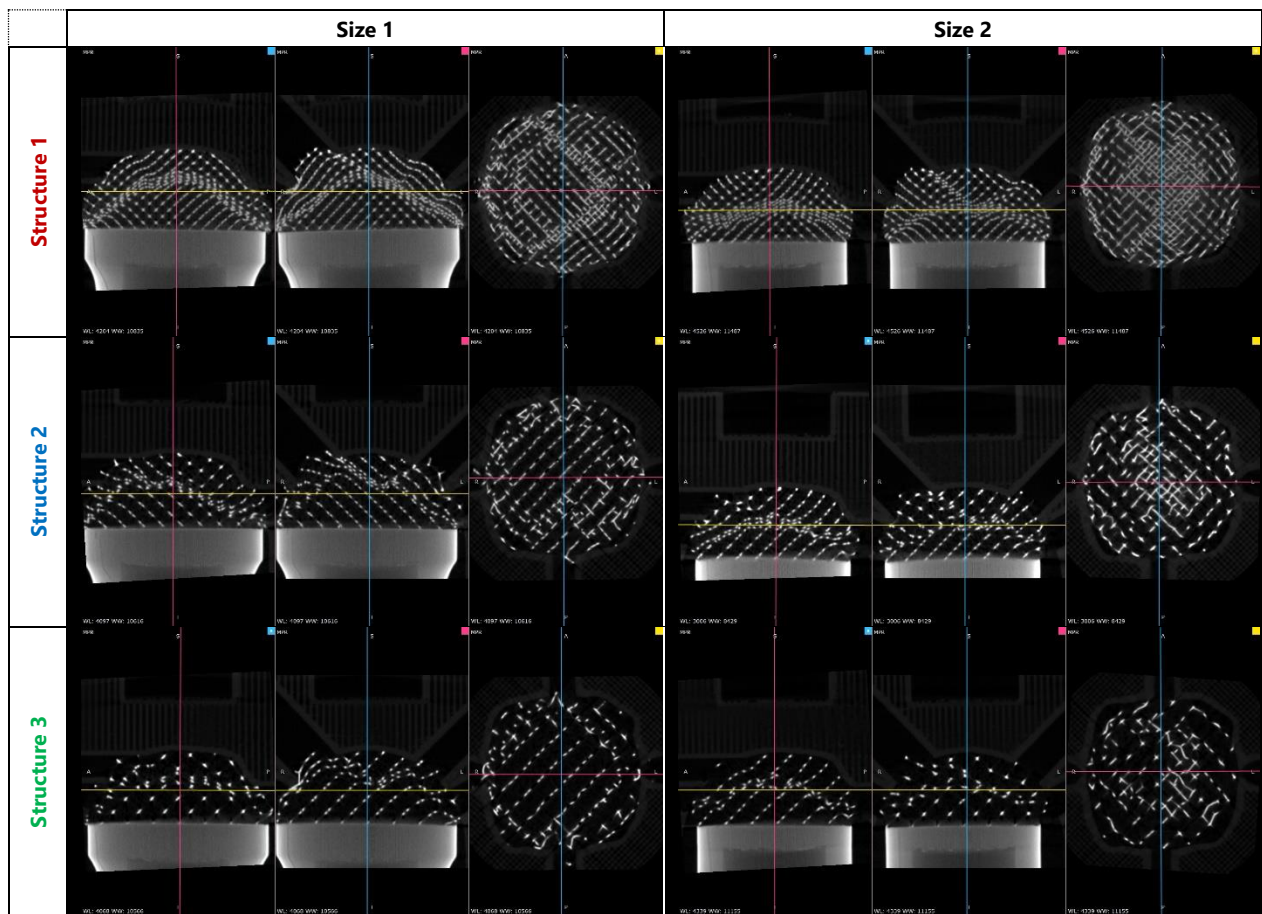


*Fig. 25 Multiplanar images of the deformed samples inside the moulds in test 2.*

Fig. 24 shows that the samples are hardly expanded, but that they are mainly compressed, except for the region near the solid part where there is some expansion visible. The images also clearly show that there is penetration into some holes, especially in the relatively larger holes at the bottom of the mould (Fig. 21). There seems to be almost no penetration into the relatively smaller and higher positioned holes.

*Pull-out test:*

The three moulds with samples from structure 1 and size 1, broke during the pull-out test at the height of the lower pin (Fig. 26). These moulds were broken before the samples could be removed. The remaining thirteen samples (with structure 1-size 2 and with structures 2 and 3) could all be pulled out the moulds (Fig. 27).

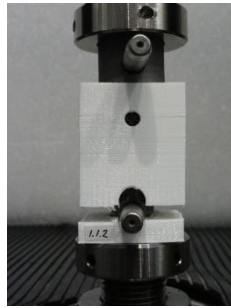


**Fig. 26** Mould broken by samples with structure 1 and size 1.



**Fig. 27** Sample removed from mould.

The results from the pull-out test are shown in Fig. 28 and Fig. 29. These figures show only the results up to the extension of 5 mm, because the load was about zero after that extension of all samples. The results over the full extension range of 10 mm can be found in Appendix C.

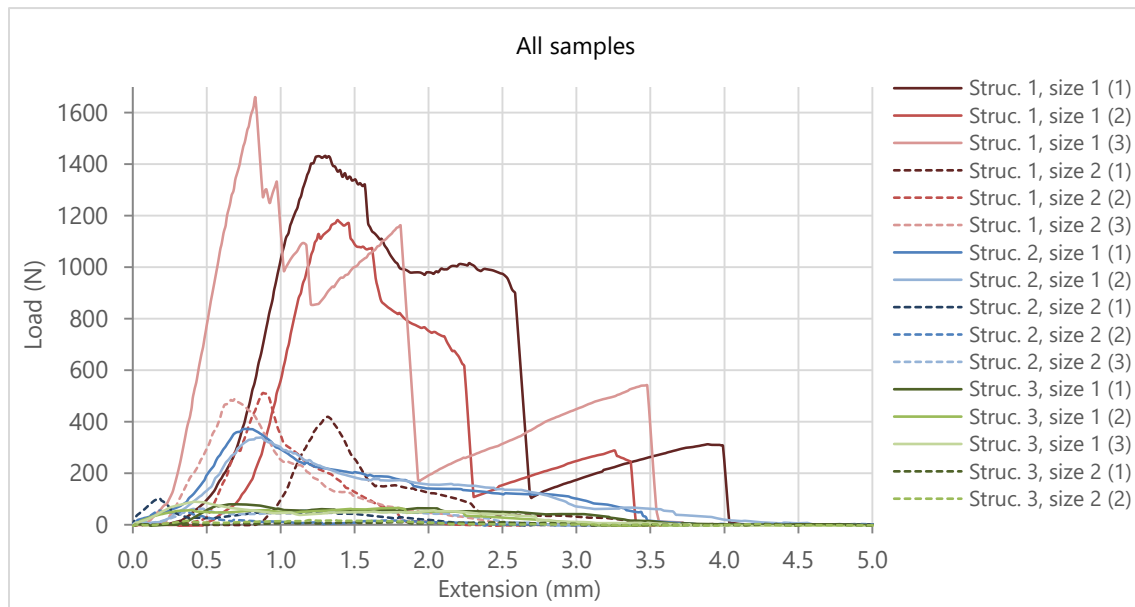


**Fig. 28** Pull-out results of all samples in test 2.

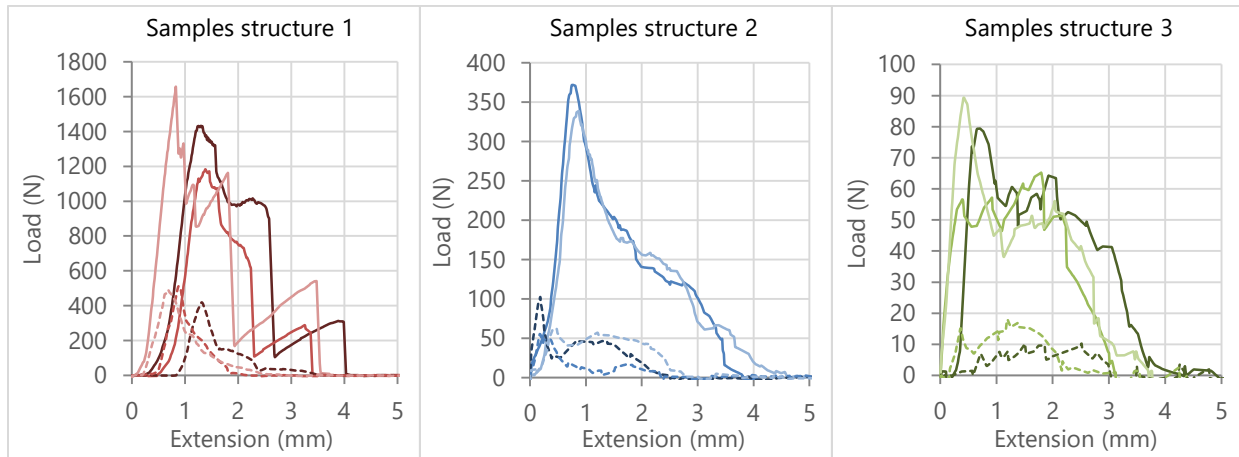


**Fig. 29** Pull-out results of the samples per structure (from left to right: structure 1, 2, and 3) in test 2.

Quite consistent results were obtained per type, except for the results of the samples with structure 1. The steep declines in the data of 'structure 1-size 1' clearly shows the breaking load of the moulds.

Similar to the push-in test, the loads are the highest for the samples with structure 1 and the lowest for the samples with structure 3. The pull-out force is the least constant over the extension for the samples with structure 3. There are again clear differences between the two sizes per structure, in which the loads are higher for the samples in size 1 compared to size 2. There is some overlap between the different sizes from different structures: the pull-out loads from 'structure 1-size 2' are somewhat similar to the loads from 'structure 2-size 1', as are the results from 'structure 2-size 2' to the results from 'structure 3-size 1'.

### 3.2.3. Discussion

The ideal mechanical properties of the implant are difficult to define and depend on multiple factors. What should be considered are the mechanical properties of the bone, the required mechanical strength of prevent failure, and the that the surgeon will be able to apply enough force to deform the implant during surgery. The mechanical properties of the implant should match the mechanical properties of the acetabular bone to redistribute the loads and avoid stress shielding. The compressive modulus of acetabular trabecular bone is about 0.0418-0.0622 GPa [35], so a relative low elastic modulus of the implant is required. On the other hand, a relatively high mechanical strength is needed to prevent mechanical failure under compression.

To provide both a low elastic modulus and high mechanical strength, the structure should probably be designed with a gradient porosity. This was also done in the study of Wang et al. [36], in which a graded acetabular cup was designed with a high porosity at the bone-implant interface and a solid material at the joint surface. The elastic modulus was gradually changed from 1.0 GPa (equal to the average elastic modulus of spongy ilium bone) to 110 GPa (solid Ti-6Al-4V). The required strength on the inner layer (joint side) was set to a minimum of 500 MPa. [36] Based on these requirements, the implant designed in this study would preferably have a minimal strength of 500 MPa and an elastic modulus between 0.5 GPa (based on the compressive modulus of acetabular bone) and 103 GPa (bulk elastic modulus of pure titanium).

In addition to a minimum required strength, there is also a maximum required strength. The maximal forces that are needed to deform the implant, will be restricted by the forces the surgeon can apply and by the forces that acetabular bone can handle. The host bone should not break during or after the operation. West and Fryman [37] measured the impact forces for the insertion of press-fit acetabular cups during a cadaveric study. The maximum and average impact force magnitudes were 27,490 N and 16,750 N, respectively. How much force the bone can handle is patient specific and depends among others on the quality of the bone, the thickness distributions, and the presence of large defects. Since the new implant will

be implemented by patients with massive acetabular defects, the mechanical properties of the patient's bone will probably not meet those of a healthy acetabulum.

The main objective of the test was to get an indication of the deformation behaviour and forces, and to investigate whether the structures deform under compression according to their surrounding shape. Since the surrounding structure (mould) was not of interest, it is not possible to clearly define the ideal compression forces. It is unclear how much force the deteriorated acetabular bone can handle (differs per patient) and how the forces will change when the structures are compressed in another mould or bone. The samples and moulds are not scaled to the real sizes of the implant and the acetabulum. Furthermore, the moulds have different mechanical properties than the acetabular bone, and the resulting forces on the acetabulum will therefore also be different. The effect of the mould, the holes and the sample dimension on the deformation behaviour and push-in/pull-out forces are unknown. Future samples should therefore be larger, and tested on a bigger scale and in a more realistic model, such as in a plastic acetabulum or, even better, in a cadaveric acetabulum. The deformation of the implants inside the acetabulum, the load distribution, and the implant's stability could then be tested more precisely.

To set up a cadaver study, acetabula should be harvested from cadavers. Since it will be difficult to find massively defected acetabula, intact acetabula could be harvested and processed before being used in tests. Holes and deformations could be drilled in the bone to create a representative model of a massively defected acetabulum. Micro-CT scans and segmented models of severe acetabular defects can be used to define the hole sizes and locations in the cadaver bone. Once the cadaveric acetabular bones contain massive defects, larger scaled implant designs can be tested. Just like the cadaveric study performed by Michel et al. [38], the push-in forces could be measured using a hammer instrument with force sensor, and the pull-out forces could be measured in a tangential pull-out test. To measure the load distribution, pressure sensitive tape could be used, for example.

The ideal cellular structure has a low push-in force (to easily deform it without breaking the host bone) and a high pull-out force (to increase the initial stability). But the results show that the push-in and pull-out forces are positively correlated, so the optimal balance between these two forces should be found. When only comparing the push-in and pull-out forces of the tested structures, structure 2 seems to be the most interesting structure of the three. This is probably, because the structure is highly deformable with relatively low push-in forces, just like structure 3. In addition, the pull-out force of structure 2 is higher than for structure 3. Nevertheless, only one highly porous structure, such as structure 2, will not be sufficient for the final implant to meet all mechanical requirements. As mentioned before, a gradient porosity will be needed in which several structures are combined, and this will therefore be an important topic for further research.

The push-in curves in Fig. 22 show peaks and valleys. This might be caused by a layer-by-layer deformation mechanism, in which the deformation takes place per stroke of unit cells. The load drops when a layer of unit cells collapses and increases after the loads are transferred to the next layer of unit cells. This deformation process cannot be observed on the micro CT-scans, because the scans only show the deformation at the end of the push-in test. To make the deformation process more visible, another test will be performed in which several micro-CT scans will be made during the push-in process. This test can be found in section 3.3.

The pull-out forces of the samples from 'structure 1-size 1' are unknown, since the moulds broke before the samples were fully removed. However, it can be concluded that the pull-out forces of structure 1 are at least three times higher than the pull-out forces of structures 2 and 3. It is therefore expected that initial stability is the highest for structure 1.

Fig. 24 shows that the samples are mainly compressed and that there was almost no expansion. Another unit cell type could possibly result in more expansion, but this is not necessarily needed. The tested samples are deformed according to the surrounding shape and even penetrated into some of the holes. The samples therefore fixated themselves without the need of expansion.

Some struts got stuck in the mould during the push-in test. This could have resulted in higher pull-out forces, which would not occur on a real implant-bone interface. However, it would be possible that the struts of the final implant get stuck inside the bone, but this should be checked in a cadaver study.

#### **3.2.4. Conclusion**

Seventeen samples were printed using three different structures and two different sizes. They were compressed into a mould, scanned with a micro-CT scanner, and subsequently pulled out. The results were promising, because all samples deformed according to their surrounding shape and penetrated into some of the holes. Most penetration occurred in the larger holes, which were located more to the bottom of the mould. Ideally, the structure has a low push-in force and a high push-out force, but it turned out that these forces are positively correlated. Therefore, structure 2 (unit cell size 3x3x3 mm) seems to be the most interesting structure of the three different structures, because it has a lower push-in force than structure 1 and a higher pull-out force than structure 3. However, a gradient porosity is needed to ensure that the implant meets all the mechanical requirements while keeping the acetabular bone intact. Therefore, more advanced research is needed to examine the possibilities of a gradient porosity and to test samples on a larger scale in a more representative model.

### 3.3. Test 3: Push-in test – Deformation process

Eight highly porous samples were compressed into a mould. In this test, micro-CT scans were made at several small deformation intervals ( $\pm 1.1$  mm compression in the Z-direction). In this way, it was tried to get a better understanding of the deformation process of highly porous diamond cellular structures.

#### 3.3.1. Materials and methods

Porous hemispherical samples with non-porous fixture parts were produced by 3D Systems (Leuven, Belgium) with a SLM machine. The samples were made from CP titanium grade 1 and tested as manufactured, so no heat treatment was applied. The samples were printed in two different sizes (Fig. 30) and in two different structures (Fig. 31). The sizes of the porous parts were equal to the sizes of the porous parts from test 2. Structures 2 and 3 from tests 1 and 2 (see Table 3) were tested. Two samples were tested per structure and size, which means eight samples were tested in total.

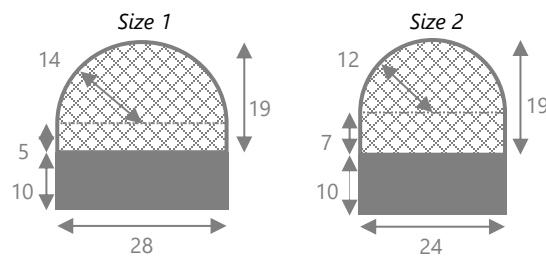


**Fig. 30** Dimensions (mm) of samples test 3.

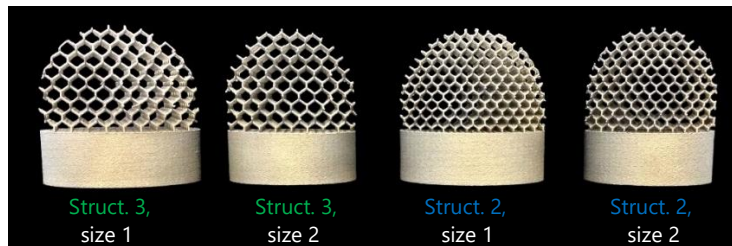


**Fig. 31** Porous samples of test 3.

The moulds (Fig. 32) for this test were comparable to the moulds from test 2. They had the same holes and deformations, but the mould was shorter and circular instead of squared. The moulds were again designed using Solidworks 2017 and Geomagic Freeform Plus software. In total, eight moulds were printed with an Ultimaker 2+ and Ultimaker 3 from PLA with 50% infill.



**Fig. 32** Mould of test 3.

To enable the gradual deformation of the samples in between the scans, the moulds and samples were placed in PVC parts with screw threads (Fig. 33). The parts were made from non-metal material (PVC) and

ordered from the online store PVC Voordeel (WitWay Webshops B.V., Drachten, Netherlands). The holders were hollowed to make sure that the moulds would fit in.



**Fig. 33** PVC parts (cap and holder) with mould and sample.

The micro-CT scans were performed on a Caliper LifeSciences Quantum FX micro-CT scanner with 90 kV and 200  $\mu$ A. Two scans were made per sample per position (90 kV, 200  $\mu$ m): one to measure the inner distance between the cap and the holder (FOV: 60 mm, time: 17 sec., voxel size: 118  $\mu$ m<sup>3</sup>), and another scan to examine the porous part of the sample (FOV: 30 mm, time: 3 min, voxel size: 59  $\mu$ m<sup>3</sup>).

The eight samples were tested one after the other, and the same steps were taken for each sample. The mould was placed in a holder, after which the sample was placed in the mould. The cap was tightened till it touched the sample. This was the starting position of the test. Two scans were made of the sample in this position.

Subsequently, the cap was tightened using a pipe wrench and vice tool. After a 180 degrees rotation of the cap, (equal to a normal displacement of 1.1 mm), the distance was measured with a calliper and two new scans were made. These steps were repeated till the cap was maximally tightened, so the inner part of the cap touched the upper part of the holder. The total displacement of the sample was about 8.1 mm.

As with test 2, the software programs ImageJ and RadiAnt DICOM viewer were used to make images of the CT-scans.

### 3.3.2. Results

The different deformation stages of one of the samples (in structure 2, size 2) have been shown in Fig. 34. The images of the remaining samples can be found in Appendix D. The side and top views are displayed per displacement, which is listed in millimetres on the left side of the image. The grey dotted lines represent the original, undeformed, shapes of the porous part.

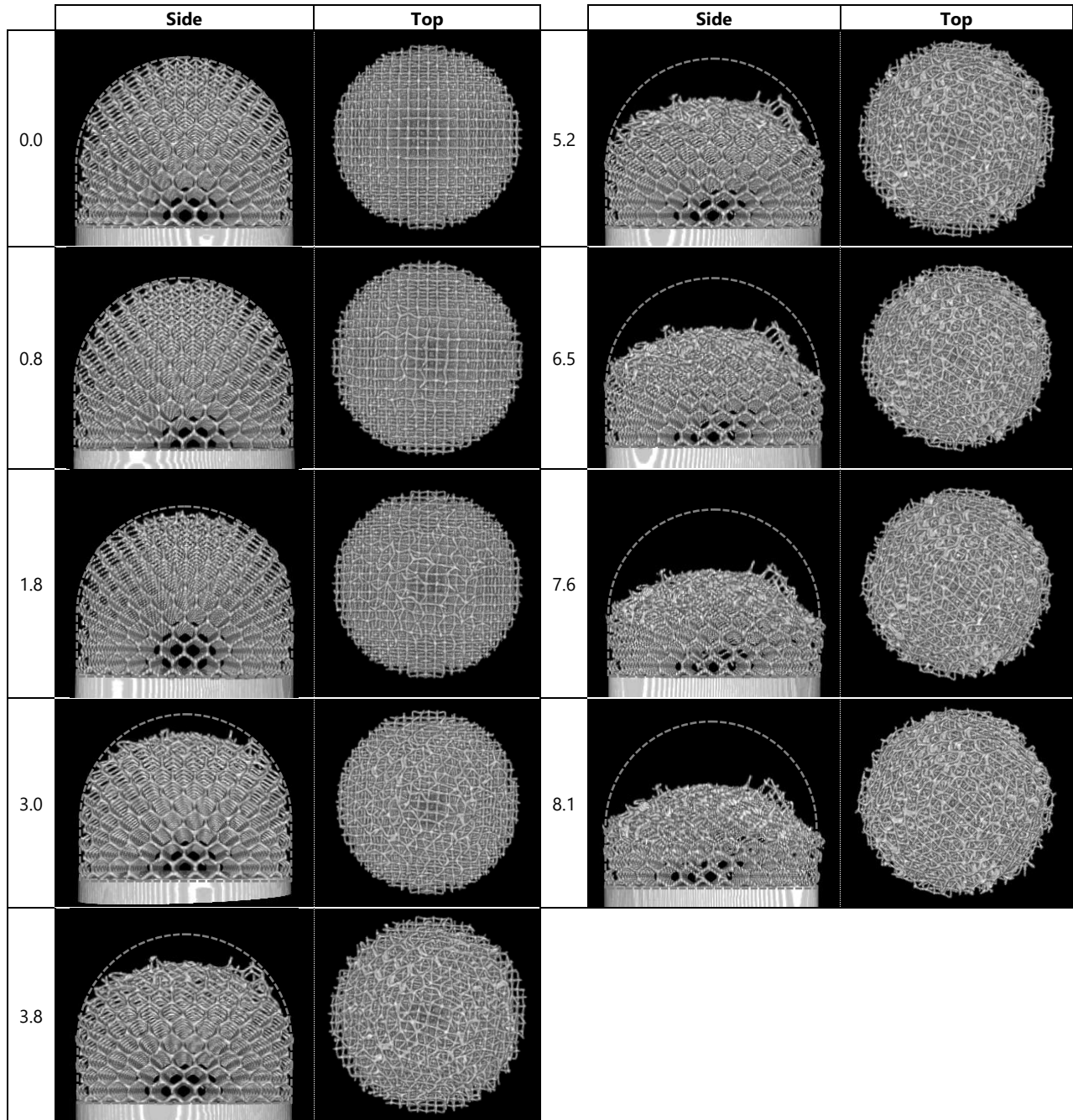


**Fig. 34** Images of the different deformation stages from sample 2.2.2 (structure 2, size 2) in test 3.

The results show that there is no equal deformation of all unit cells at the same time, instead the samples deformed gradually. The unit cells that are in direct contact with the mould deformed first. This deformation continued to the other underlying unit cells. At the same time, some penetration in the holes started. At the end of the 8.1 mm displacement, there are still some relatively undeformed unit cells in some of the samples.

All samples from the same type show a comparable deformation process. There are also no clear differences in the deformations of structure 2 and 3. All unit cells of the samples in size 1 are almost fully compressed, while the samples of size 2 often contain some less deformed, or almost undeformed, unit cells. These cells are located near the non-porous part of the sample.

In addition to the previously shown images, a link was made between the deformation curves of the push-in test from test 2 and the deformation process found in this test. Therefore, cross-sections are made of two samples: one sample of 'structure 2-size 1' (Fig. 36) and one sample of 'structure 3-size 2' (Fig. 37). Fig. 35 shows the push-in curves of test 2 with several points that correspond to the cross-sections from Fig. 36 and Fig. 37.

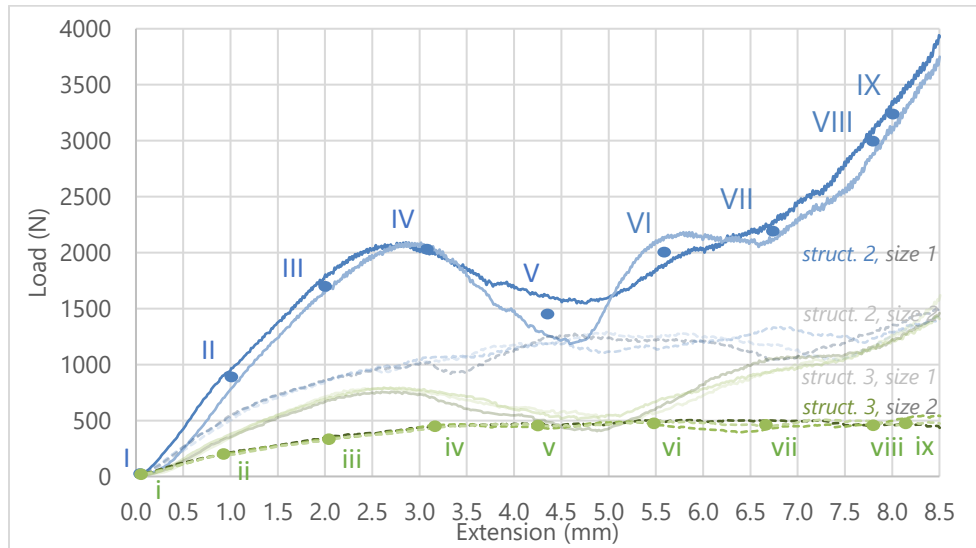


**Fig. 35** Push-in curves of test 2 with points corresponding to cross-sections of test 3.

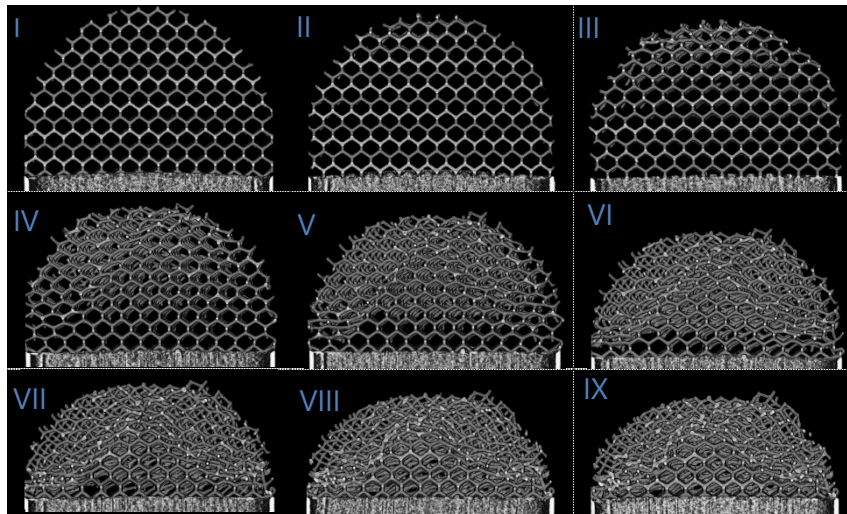


**Fig. 36** Cross-sections of sample structure 2, size 1 (test 3).

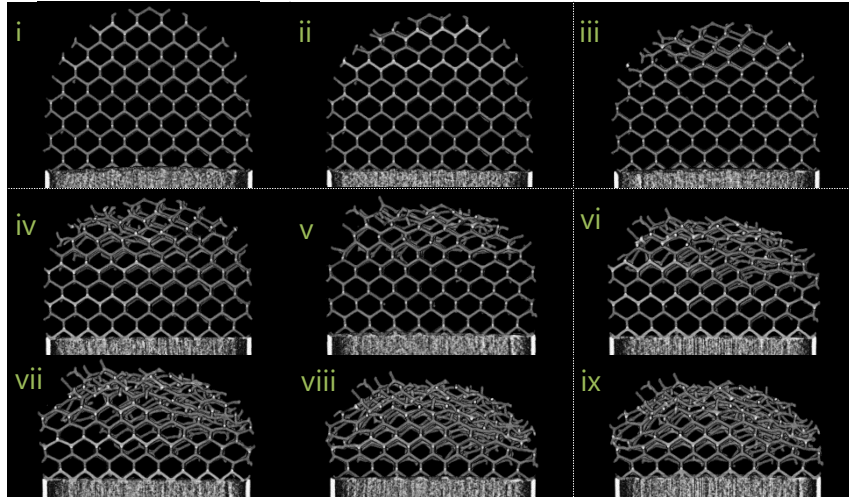


**Fig. 37** Cross-sections of sample structure 3, size 2 (test 3).

### 3.3.3. Discussion

The results of this test confirm the assumption that the unit cells do not deform all at once but in difference stages. The images of Fig. 34, Fig. 36, and Fig. 37 clearly show a gradual deformation, in which some of the unit cells almost stay undeformed at the end of the test. The peaks and valleys in structure 1-size 1 cannot be clearly derived from the images, but there are some large deformation differences visible between images III, IV, and V, that could correspond to the initially flat and then sharp decrease of the push-in curve.

The images of test 3 are compared with the curves of test 2. These results roughly match, and it gives a good impression of the deformation process along the push-in curve. There are, however, some differences between the push-in tests of test 2 and 3. There was for example no constant compression speed in test 3 and the speed was in general much higher than the speed of test 2. In addition, there was a small rotational force in test 3, which was caused by the cap being turned on the holder to push the sample into the mould. This resulted in some slightly rotated unit cells, especially the unit cells that were in direct contact to the mould.

The forces on the cap and holder increased every time the cap was tightened. As a result, the inside of the cap started to dimple a little. The actual deformation of the samples might therefore be slightly smaller than the measured deformations.

It was difficult to fit the larger samples (size 1) in the FOV of 30 mm, since there was only a small margin between the sample size ( $d=28$  mm) and FOV (30 mm), and the samples had to be moved manually without a live CT viewer. A FOV of 40 mm was also considered, but these images were not sharp enough. As a result, there are a few scans that miss a small piece of the samples. This was limited as much as possible, but fortunately these small missing pieces are unnecessary to analyse the deformation process.

### 3.3.4. Conclusion

The goal of this test was to visualize the deformation process of highly porous pure titanium structures. Therefore, eight porous samples were printed in two structures (2 and 3) and two sizes (sizes 1 and 2). The samples were manually compressed in a mould and after each deformation (1.1 mm) a micro-CT scan was made. This was continued up to a total displacement of about 8.1 mm. Side view, top view, and cross-section images were made of the samples and compared with the push-in results of test 2.

The images clearly show the deformed samples and the deformation process. As already expected, the unit cells of the cellular structures do not deform all at once, but in different stages. The deformation of the unit cells decreases from the cells that are in direct contact with the mould to the unit cells near the solid part of the sample. The penetration of the samples into the holes occurs gradually during the deformation.

## 4. DISCUSSION

### *Main observations:*

The mechanical properties and deformation possibilities of highly porous pure titanium samples were investigated in this study. The focus lies on the plastic deformations of the structures and on how the samples deformed under compression.

The results show that there are large plastic deformations possible with the highly porous structures. The theoretical bending properties of the diamond unit cell are investigated by combining analytical and experimental mechanical properties of diamond cellular structures. It was found that it is almost impossible to obtain larger plastic deformations using a larger strut length than those used in structures 2 and 3 (1.18 and 1.62 mm, respectively). The measured plastic deformation at the plateau end for structure 3 is about 61%, and a maximum theoretically achievable plastic deformation is about 61.2%, when the structure is deformed up to the plateau end. This is because the elastic modulus decreases if the strut length increases. Subsequently, the increase in plastic deformation is smaller than the increase in elastic deformation.

Test 2 showed that the porous structures can deform according to their surrounding shape. The push-in and pull-out forces differ per structure and size: the more porous and bigger the sample, the higher the push-in and the pull-out forces. A low push-in force is preferred to deform the implant, while a high pull-out is preferred to indicate a better initial fixation.

The push-in test of test 2 and the micro-CT scans of test 3 shows that the unit cells do not deform equally under compression. There is a gradual deformation visible, showing a layer-by-layer compression, in which the unit cells in contact with the mould deform first, while the deformation slowly moves towards the unit cells close to the solid part of the sample.

### *Future research:*

Some suggestions on further research were already given in the aforementioned discussions. One of the suggestions is to investigate the most optimal unit cell geometry. The diamond cell was used in this research, but there is perhaps a more suitable unit cell that can achieve larger plastic deformations. One could, for example, look at unit cell types with higher Poisson's ratios, to obtain a larger horizontal expansion of the structure. The structure may then be able to increase its initial fixation.

In addition to the unit cell type, attention should be paid to a gradient porosity. This will able the implant to be strong enough and still highly deformable. There are many design possibilities that should be considered, which will make it a complex study. Some variations that can be investigated are the combination of unit cell types, unit cell sizes, strut thicknesses, and the connections between the unit cells. This will all influence the mechanical properties of the structure.

As mentioned in the discussion of test 1, the samples are not heat treated because it was assumed that this would have a negligible influence on the mechanical properties of the thin struts. However, this assumption was not tested. Since the final implant will be heat treated, it is recommended to heat treat all future test samples to check this assumption. Besides, the test samples will become more advanced with some thicker struts due to the gradient porosity, for which the heat treatment most certainly will change the mechanical properties.

Another suggestion for future research is to set up a cadaver study. Testing in cadaveric bone will give more realistic results compared to the results obtained in test 2, because the samples were tested on a different scale and in a plastic mould. The influence of the mould, holes, and samples sizes on the deformation behaviour and push-in/pull-out forces are unknown. When testing porous samples on cadaveric bone, the deformation, the load distribution, and the implants stability can be tested more precisely. It will also give some insight in how the bone reacts to the compression forces and which forces the bone can handle.

With all the obtained information, a better estimation can be made about the ideal mechanical properties of the implant, which mainly depend on the stiffness and strength. The stiffness should be comparable to the bone to prevent stress shielding. And the implant should be strong enough to prevent failure of the implant, while at the same time allowing large plastic deformations without breaking of the acetabular host bone.

*Future perspectives:*

Before testing a complete new type of implant, an intermediate step may be to design and test a simplified implant. This implant does not have to be fully deformable, but it can contain only a small outside layer that is deformable. This simplified version can still have flanges to ensure the implant's stability. These flanges could be designed with a small deformable layer to make sure that there is a perfect fit after compression.

The plastically deformable implant will be patient specific. However, in the future it would be useful if this can be developed in a more general implant that comes in several sizes and shapes. It will then become an off-the-shelf implant that is deformed during the operation to create a perfect fit. This will require less time to design and manufacture the implant compared to patient specific implants. In addition, it will ease the preoperative planning and it will be cheaper compared to patient specific implants.

Another design possibility would be to combine this new type of implant with preventive measures against infections. This would be of added value to young and active patients who suffer from severe acetabular defects because of infections. This golden combination will outperform the currently available implants. The porous structure is highly suitable to carry those anti-infectious agents such as silver particles. This principle is currently under investigation within the Prosperos project.

## 5. CONCLUSION

The mechanical properties and deformation behaviour of highly porous pure titanium grade 1 structures were investigated in this study. Tests were performed on diamond cellular samples that were printed in three different porosities (theoretically 95.6%, 98.0%, 98.8%). A uniaxial compression test was performed on cylindrical samples, and push-in and pull-out tests were done on hemispherical shaped samples. These samples were printed in two sizes and compressed into moulds containing various holes based on acetabular defects. Micro-CT images were made of the samples to analyse the deformation. In addition, an analytical method was used to predict the plastic deformation of the diamond cellular structure with any combination of strut length and strut thickness.

The cylindrical samples showed large and quite constant deformations ( $> 57\%$ ). Based on the analytical and experimental results, it was found that the tested samples nearly reach the maximum plastic deformation at the plateau end for diamond cellular structures ( $\pm 61\%$ ). When increasing the strut length/thickness ratio even further ( $> 5.9$ ), hardly any additional plastic deformation will occur.

The hemispherical samples deformed conform the surrounding shape of the mould and penetrated into some holes. The push-in and pull-out forces are positively correlated and are higher for less porous structures. The micro-CT scans and push-in curves give insight into the deformation process and show that the unit cells do not equally deform, but gradually deform, layer-by-layer with compression.

These results are quite promising, and it gives confidence in the feasibility of making this new type of implant for patients with massive acetabular defects. This study can be seen as a first step towards the design of a deformable cup and it can function as a basis for future work. Future research should focus on implementing a gradient porosity using the most optimal unit cell type(s), while studying its effects in a cadaver study.

## 6. REFERENCES

1. Mäkinen, T.J., et al., *Role of cages in revision arthroplasty of the acetabulum*. JBJS, 2016. **98**(3): p. 233-242.
2. Petrie, J., A. Sassoon, and G. Haidukewych, *Pelvic discontinuity*. Bone Joint J, 2013. **95**(11 Supple A): p. 109-113.
3. Barlow, B.T., et al., *Outcomes of custom flange acetabular components in revision total hip arthroplasty and predictors of failure*. The Journal of arthroplasty, 2016. **31**(5): p. 1057-1064.
4. Saleh, K.J., et al., *Revision total hip arthroplasty with the use of structural acetabular allograft and reconstruction ring: a case series with a 10-year average follow-up*. The Journal of arthroplasty, 2000. **15**(8): p. 951-958.
5. Zehntner, M.K. and R. Ganz, *Midterm results (5.5–10 years) of acetabular allograft reconstruction with the acetabular reinforcement ring during total hip revision*. The Journal of arthroplasty, 1994. **9**(5): p. 469-479.
6. Berry, D.J. and M.E. Muller, *Revision arthroplasty using an anti-protrusion cage for massive acetabular bone deficiency*. Bone & Joint Journal, 1992. **74**(5): p. 711-715.
7. Symeonides, P.P., et al., *The Effectiveness of the Burch-Schneider antiprotrusion cage for acetabular bone deficiency: five to twenty-one years' follow-up*. The Journal of arthroplasty, 2009. **24**(2): p. 168-174.
8. Richards, C.J., D.S. Garbuz, and C.P. Duncan. *Porous Metal Augments: An Attractive Alternative for Reconstructing Large Acetabular Defects*. in *Seminars in Arthroplasty*. 2008. Elsevier.
9. Abolghasemian, M., et al., *Porous metal augments*. Bone Joint J, 2013. **95**(11 Supple A): p. 103-108.
10. Nehme, A., D.G. Lewallen, and A.D. Hanssen, *Modular porous metal augments for treatment of severe acetabular bone loss during revision hip arthroplasty*. Clinical orthopaedics and related research, 2004. **429**: p. 201-208.
11. Berend, M.E. *Uncemented Hemispherical Acetabular Components in Revision THA*. in *Seminars in Arthroplasty*. 2012. Elsevier.
12. Whaley, A.L., D.J. Berry, and W.S. Harmsen, *Extra-large uncemented hemispherical acetabular components for revision total hip arthroplasty*. JBJS, 2001. **83**(9): p. 1352-1357.
13. Garbuz, D., E. Morsi, and A.E. Gross, *Revision of the acetabular component of a total hip arthroplasty with a massive structural allograft. Study with a minimum five-year follow-up*. JBJS, 1996. **78**(5): p. 693-7.
14. Gross, A.E., D. Garbuz, and E. Morsi, *Revision arthroplasty of the acetabulum with restoration of bone stock*, in *Orthopaedic Allograft Surgery*. 1996, Springer. p. 101-111.
15. Buttaro, M.A., et al., *Acetabular revision with metal mesh, impaction bone grafting, and a cemented cup*. Clinical orthopaedics and related research, 2008. **466**(10): p. 2482-2490.
16. Schreurs, B.W., et al., *Acetabular re-revision with impaction bone grafting and a cemented polyethylene cup; a biological option for successive reconstructions*. Hip International, 2015. **25**(1).
17. Goodman, G. and C. Engh Jr, *The custom triflange cup*. Bone Joint J, 2016. **98**(1 Supple A): p. 68-72.
18. Holt, G.E. and D.A. Dennis, *Use of custom triflanged acetabular components in revision total hip arthroplasty*. Clinical orthopaedics and related research, 2004. **429**: p. 209-214.
19. Paprosky, W.G., P.G. Perona, and J.M. Lawrence, *Acetabular defect classification and surgical reconstruction in revision arthroplasty: a 6-year follow-up evaluation*. The Journal of arthroplasty, 1994. **9**(1): p. 33-44.
20. D'antonio, J.A., et al., *Classification and management of acetabular abnormalities in total hip arthroplasty*. Clinical orthopaedics and related research, 1989. **243**: p. 126-137.
21. Christie, M.J., et al., *Bridging massive acetabular defects with the triflange cup: 2-*

- to 9-year results. *Clinical orthopaedics and related research*, 2001. **393**: p. 216-227.
22. Dennis, D.A., *Management of massive acetabular defects in revision total hip arthroplasty*. *The Journal of arthroplasty*, 2003. **18**(3): p. 121-125.
  23. Baauw, M., G.G. van Hellemond, and M. Spruit, *A custom-made acetabular implant for Paprosky type 3 defects*. *Orthopedics*, 2017. **40**(1): p. e195-e198.
  24. Berasi, C.C., et al., *Are custom triflange acetabular components effective for reconstruction of catastrophic bone loss? Clinical Orthopaedics and Related Research®*, 2015. **473**(2): p. 528-535.
  25. Li, H., et al., *Custom acetabular cages offer stable fixation and improved hip scores for revision THA with severe bone defects*. *Clinical Orthopaedics and Related Research®*, 2016. **474**(3): p. 731-740.
  26. DeBoer, D.K., et al., *Revision total hip arthroplasty for pelvic discontinuity*. *JBJS*, 2007. **89**(4): p. 835-840.
  27. Huiskes, R., H. Weinans, and B. Van Rietbergen, *The relationship between stress shielding and bone resorption around total hip stems and the effects of flexible materials*. *Clinical orthopaedics and related research*, 1992. **274**: p. 124-134.
  28. Nine, M.J., et al., *Wear debris characterization and corresponding biological response: artificial hip and knee joints*. *Materials*, 2014. **7**(2): p. 980-1016.
  29. Arabnejad, S., et al., *High-strength porous biomaterials for bone replacement: A strategy to assess the interplay between cell morphology, mechanical properties, bone ingrowth and manufacturing constraints*. *Acta biomaterialia*, 2016. **30**: p. 345-356.
  30. Wang, X., et al., *Topological design and additive manufacturing of porous metals for bone scaffolds and orthopaedic implants: a review*. *Biomaterials*, 2016. **83**: p. 127-141.
  31. Wauthle, R., et al., *Revival of pure titanium for dynamically loaded porous implants using additive manufacturing*. *Materials Science and Engineering: C*, 2015. **54**: p. 94-100.
  32. Ahmadi, S., et al., *Mechanical behavior of regular open-cell porous biomaterials made of diamond lattice unit cells*. *Journal of the mechanical behavior of biomedical materials*, 2014. **34**: p. 106-115.
  33. Standard, I., *ISO 13314: 2011 (E)(2011) Mechanical testing of metals—ductility testing—compression test for porous and cellular metals*. Ref Number ISO. **13314**(13314): p. 1-7.
  34. Ahmadi, S.M., et al., *Additively manufactured open-cell porous biomaterials made from six different space-filling unit cells: The mechanical and morphological properties*. *Materials*, 2015. **8**(4): p. 1871-1896.
  35. *EduPack*, Granta Design Limited, Cambridge, UK, 2017. 2017.
  36. Wang, H.V., S.R. Johnston, and D.W. Rosen. *Design of a graded cellular structure for an acetabular hip replacement component*. in *17th solid freeform fabrication symposium*. 2006.
  37. West, C. and J.C. Fryman. *Cadaveric measurement of impact force on total hip arthroplasty surgical instrumentation*. in *Am Soc Biomech Conference*. 2008.
  38. Michel, A., et al., *Assessing the Acetabular Cup Implant Primary Stability by Impact Analyses: A Cadaveric Study*. *PLoS one*, 2016. **11**(11): p. e0166778.

## APPENDIX A: Test 2 - Figures of push-in test per structure

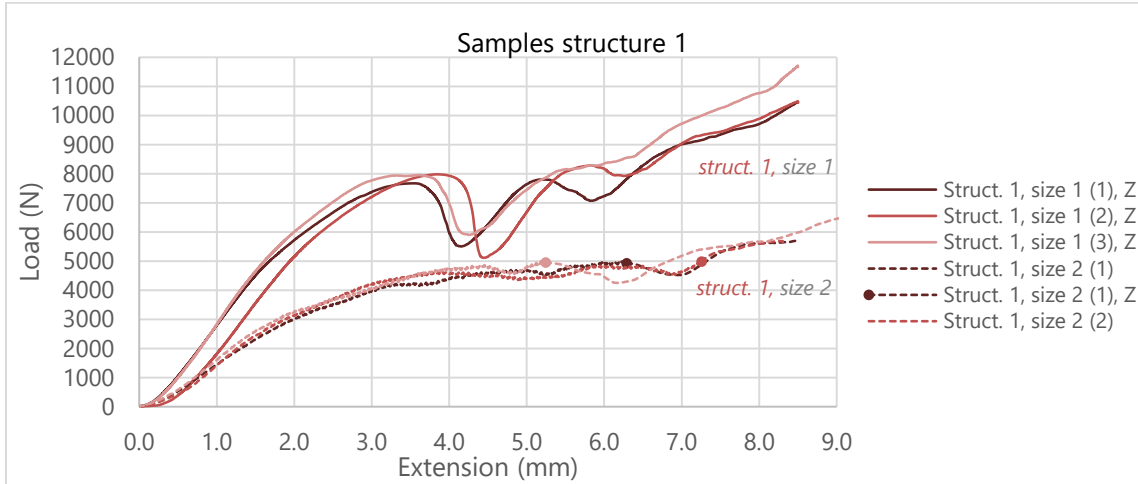


**Fig. 38** Push-in test: extension vs. load of samples with structure 1 in test 2.

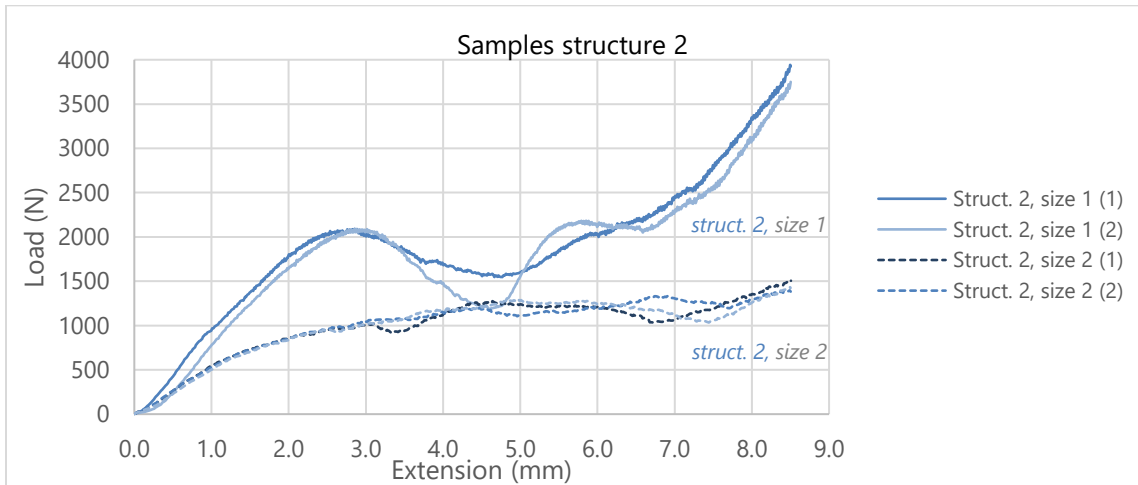


**Fig. 39** Push-in test: extension vs. load of samples with structure 2 in test 2.

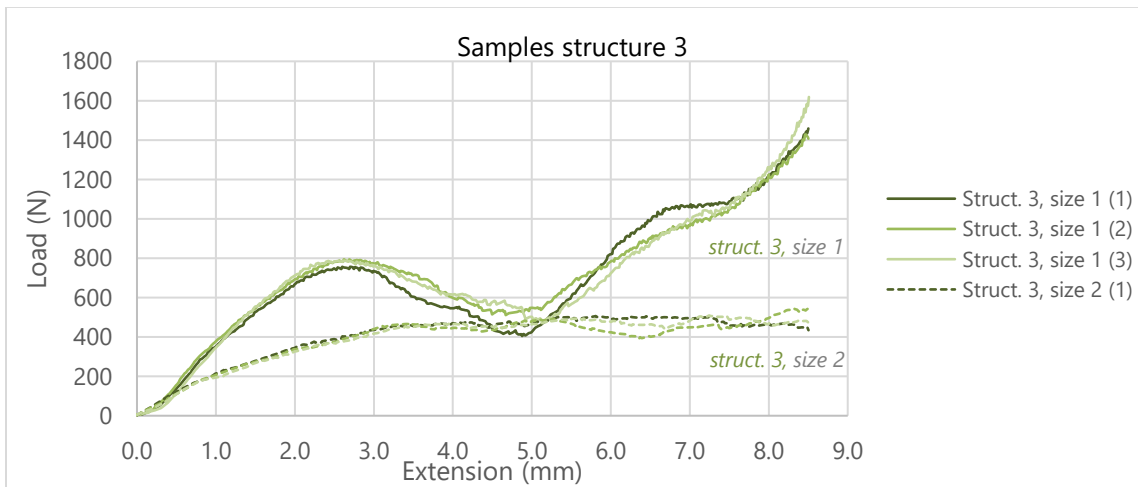


**Fig. 40** Push-in test: extension vs. load of samples with structure 3 in test 2.

## APPENDIX B: Test 2 - Micro-CT images of all samples

In this appendix are the micro-CT images of all samples shown. Fig. 41, Fig. 42, and Fig. 43 show multiplanar images that are made with RadiAnt DICOM Viewer Software, and Fig. 44 and Fig. 45 show images that are made with ImageJ software.

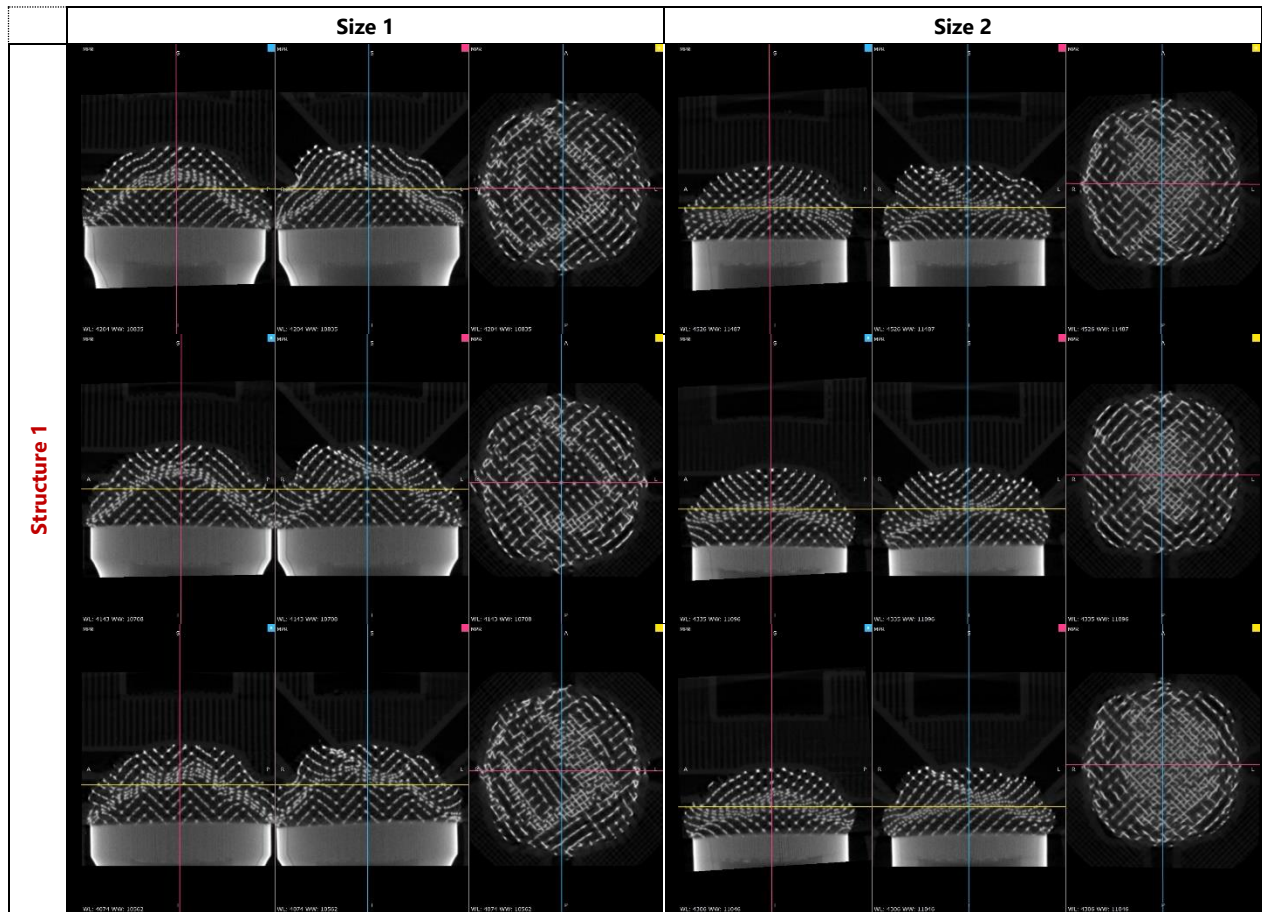
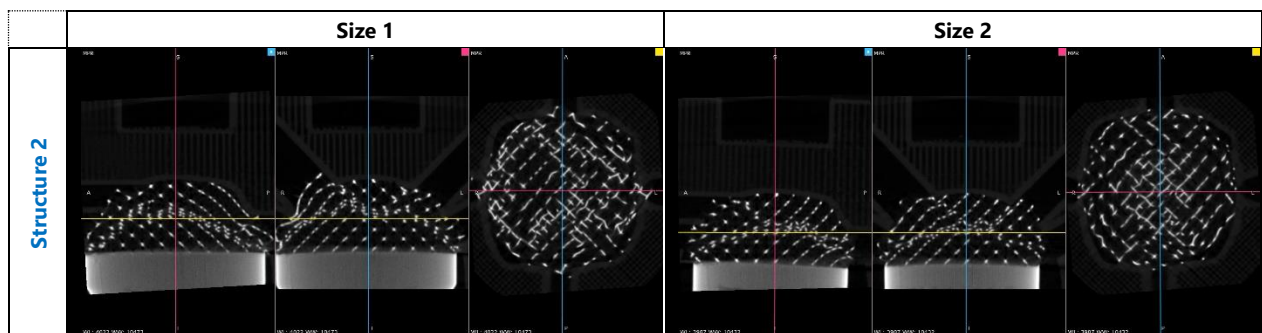


Fig. 41 Multiplanar images of the deformed samples with structure 1 into the moulds (test 2).



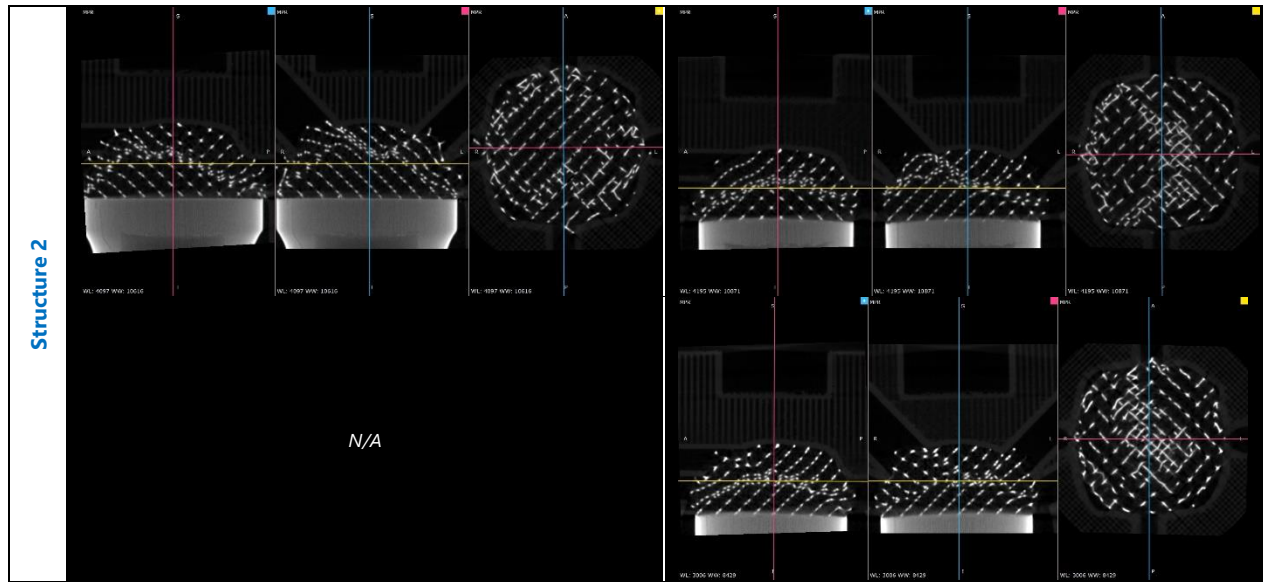


Fig. 42 Multiplanar images of the deformed samples with structure 2 into the moulds (test 2).

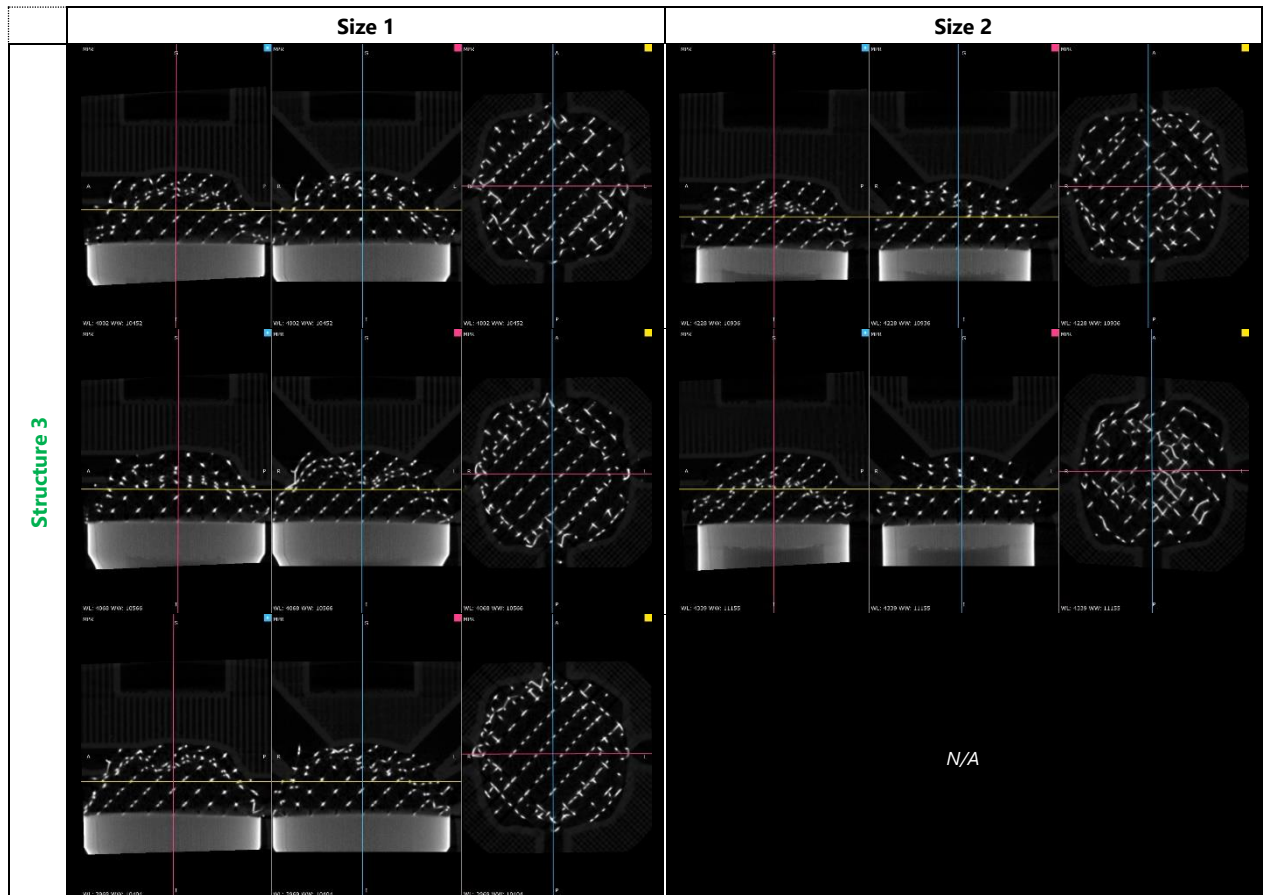


Fig. 43 Multiplanar images of the deformed samples with structure 3 into the moulds (test 2).

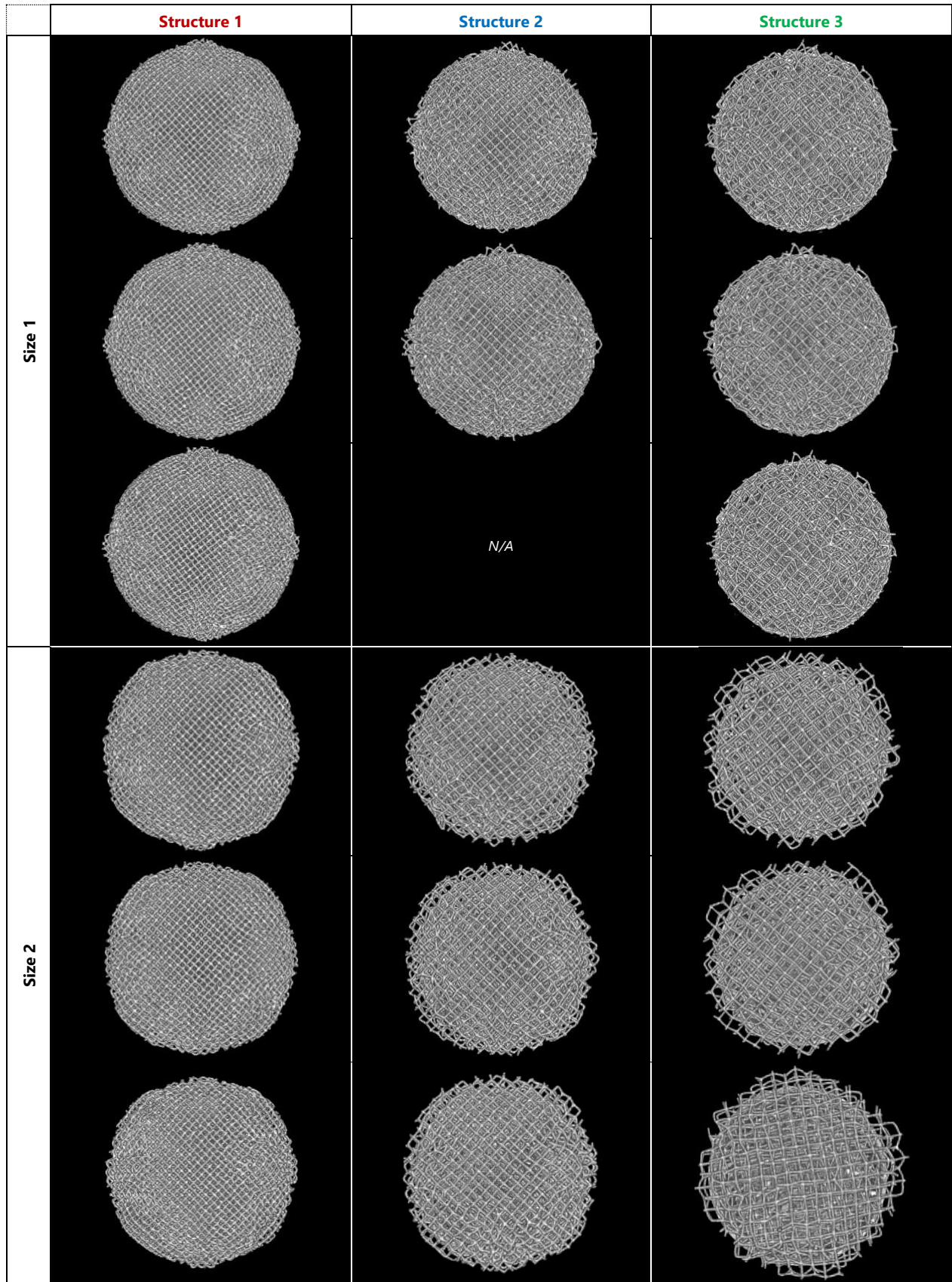
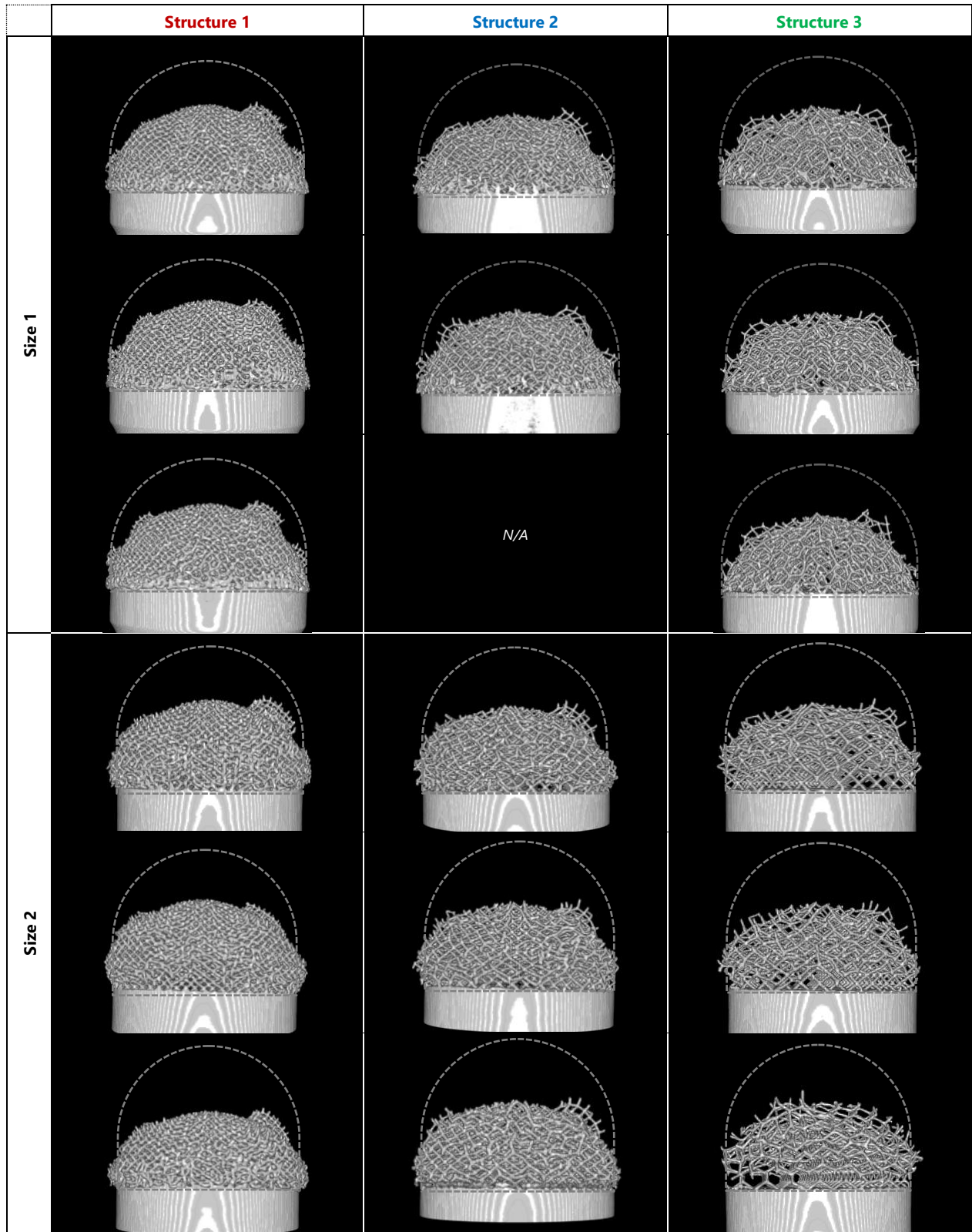


Fig. 44 Images of deformed samples in test 2, top view.



**Fig. 45** Images of deformed samples in test 2, side view.

## APPENDIX C: Test 2 - Figures of pull-out test

The results of the pull-out test are shown in Fig. 46, in which the full extension range (0-10 mm) is shown.

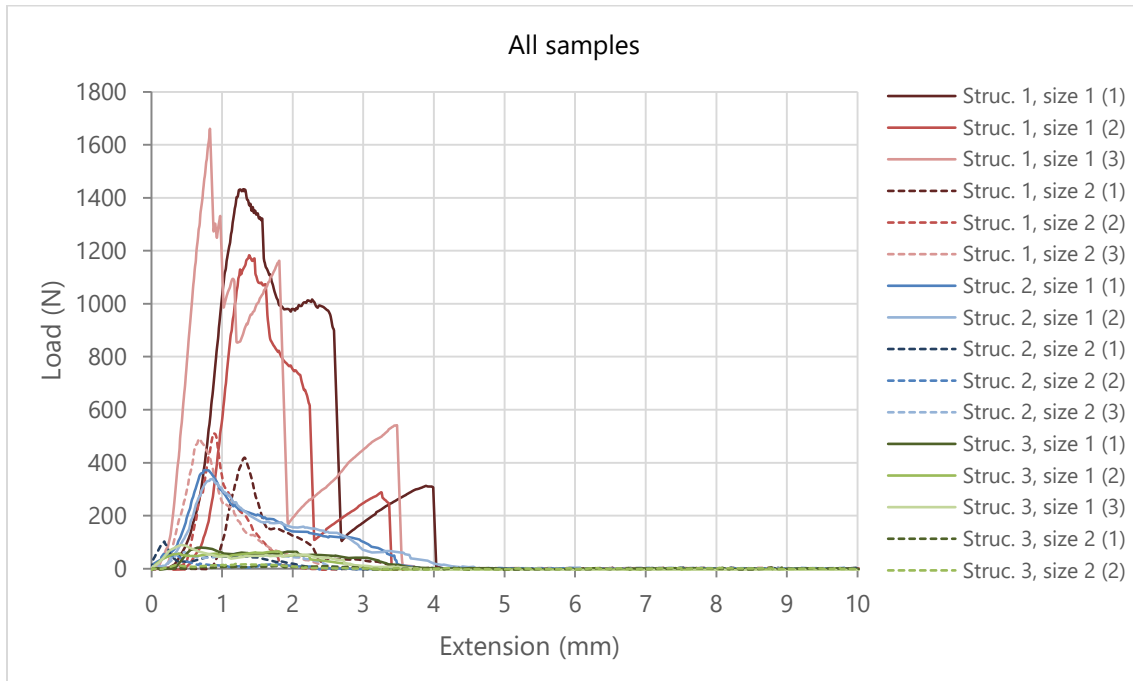


**Fig. 46** Pull-out results of all samples in test 2, full extension displayed.

The results per structure are also shown in separate figures, see Fig. 47, Fig. 48, and Fig. 49.

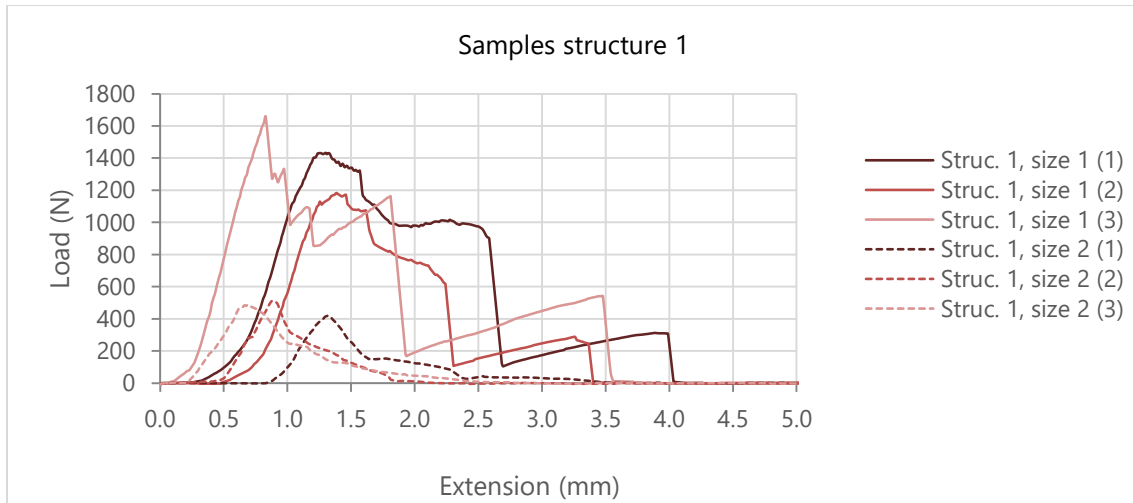


**Fig. 47** Pull-out test: extension vs. load of samples with structure 1 in test 2.

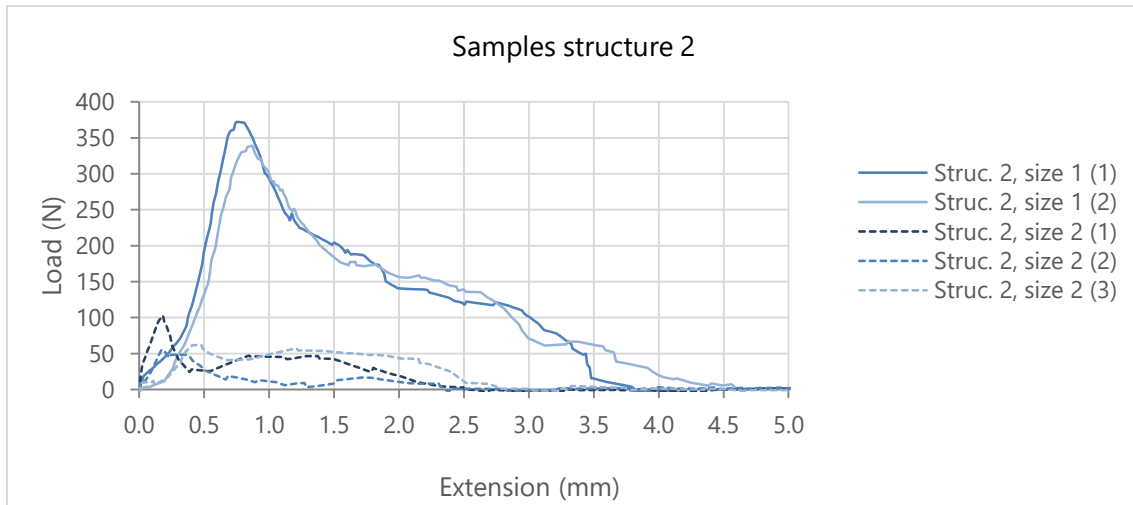


**Fig. 48** Pull-out test: extension vs. load of samples with structure 2 in test 2.

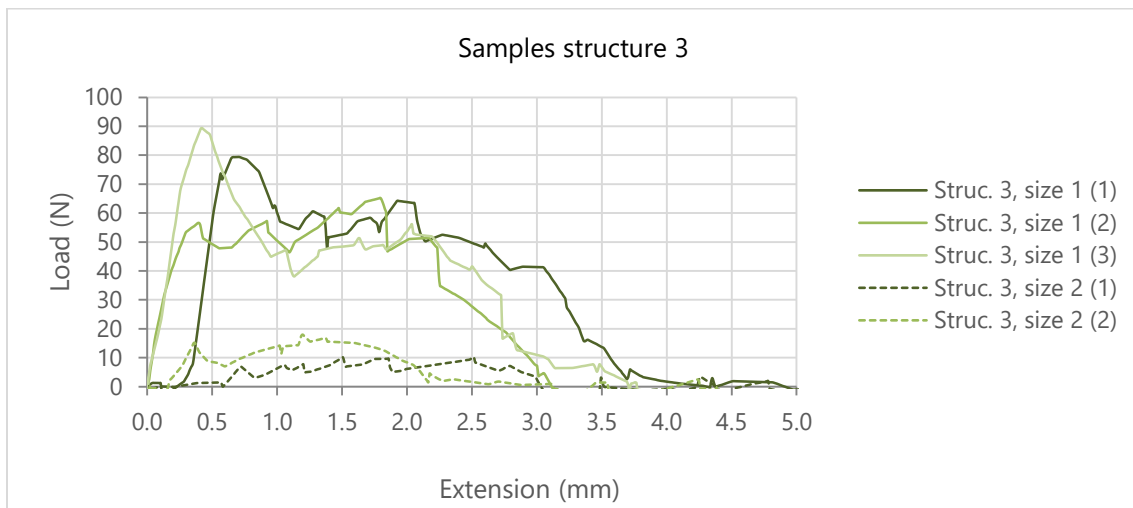


**Fig. 49** Pull-out test: extension vs. load of samples with structure 3 in test 2.

**APPENDIX D: Test 3 - Micro-CT images of all samples**

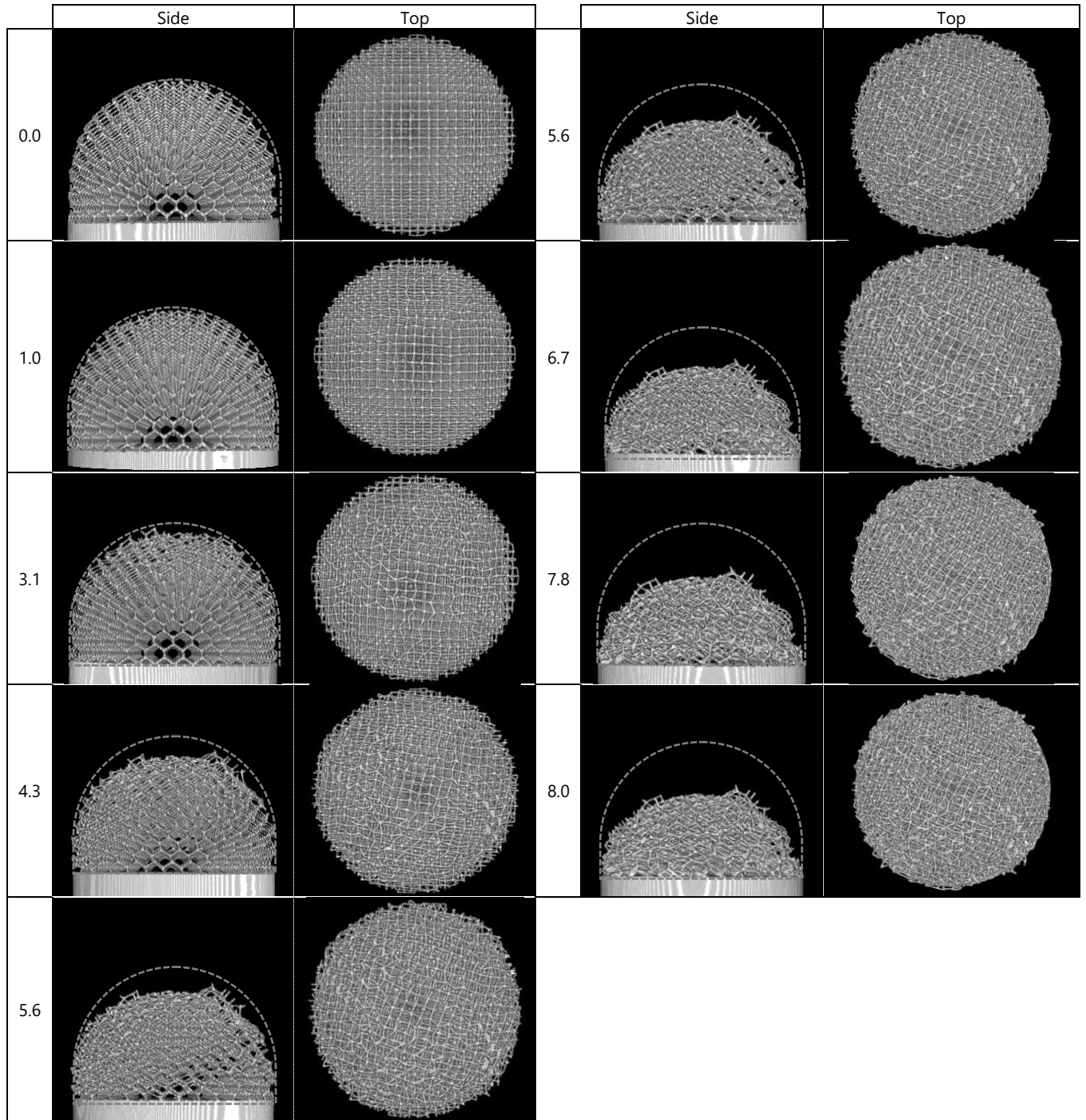


*Fig. 50 Sample 2.1.1 (structure 2, size 1) of test 3.*

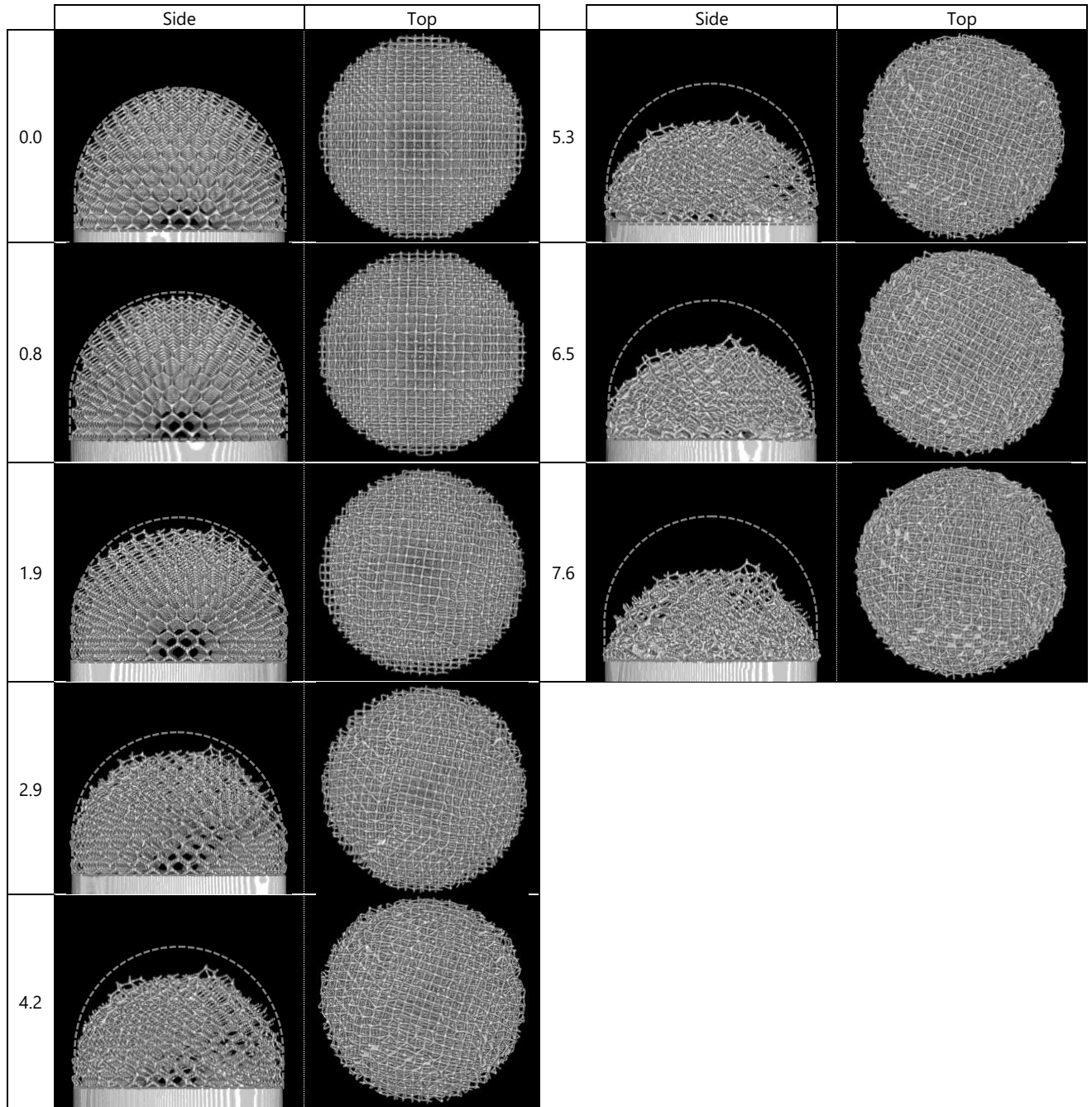


*Fig. 51* Sample 2.1.2 (structure 2, size 1) of test 3.

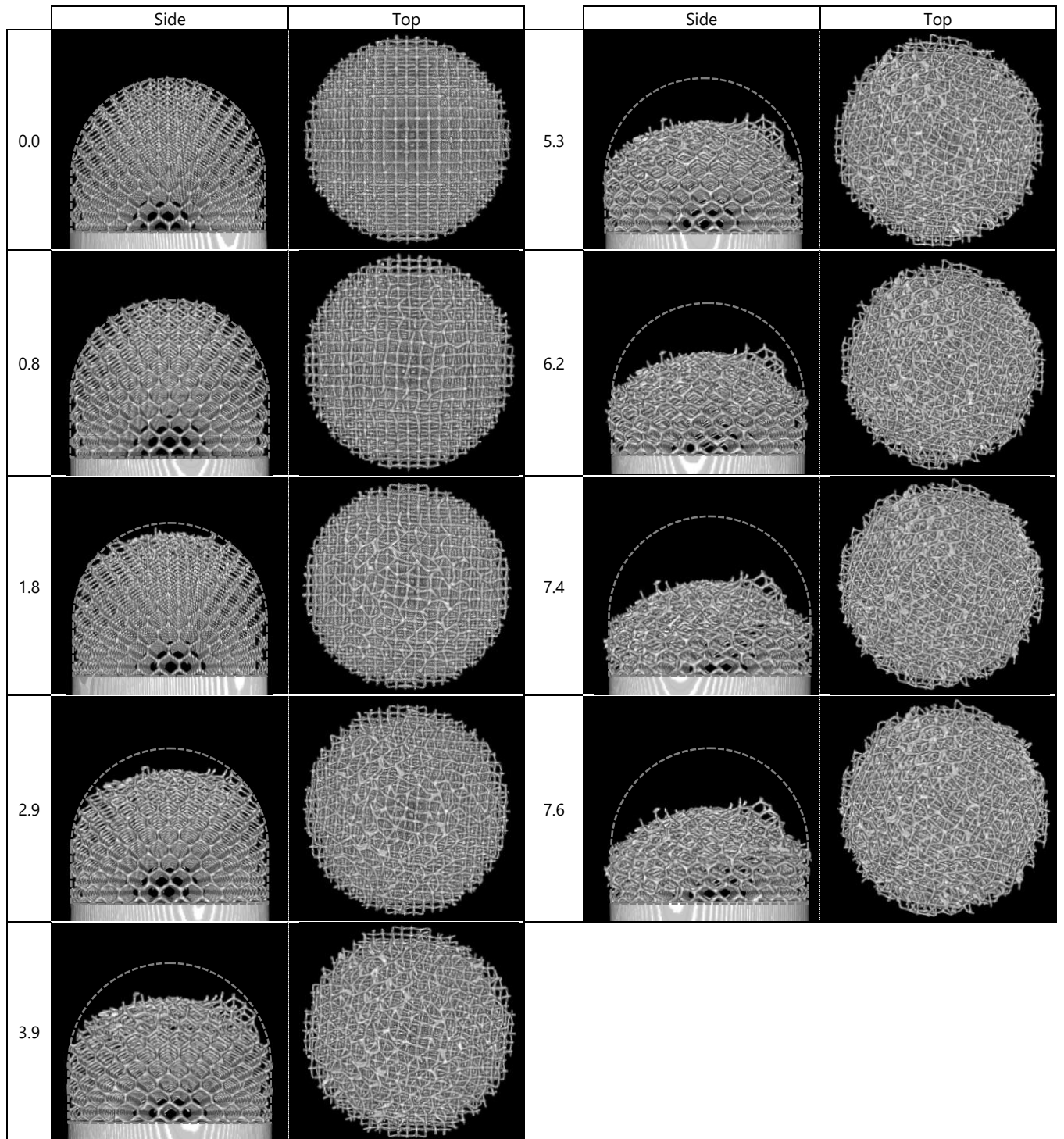


*Fig. 52* Sample 2.2.1 (structure 2, size 2) of test 3.

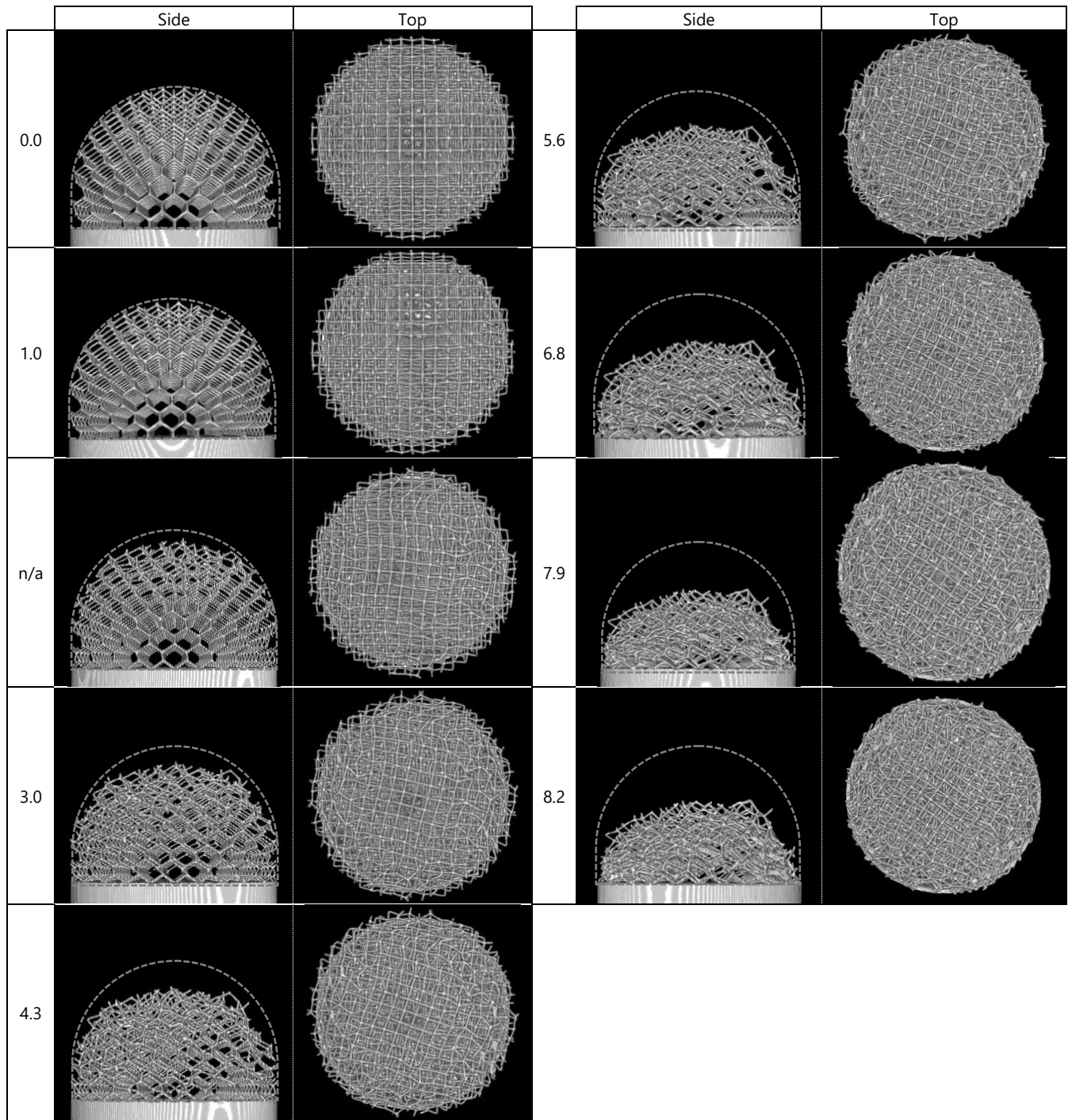


**Fig. 53** Sample 3.1.1 (structure 3, size 1) of test 3.

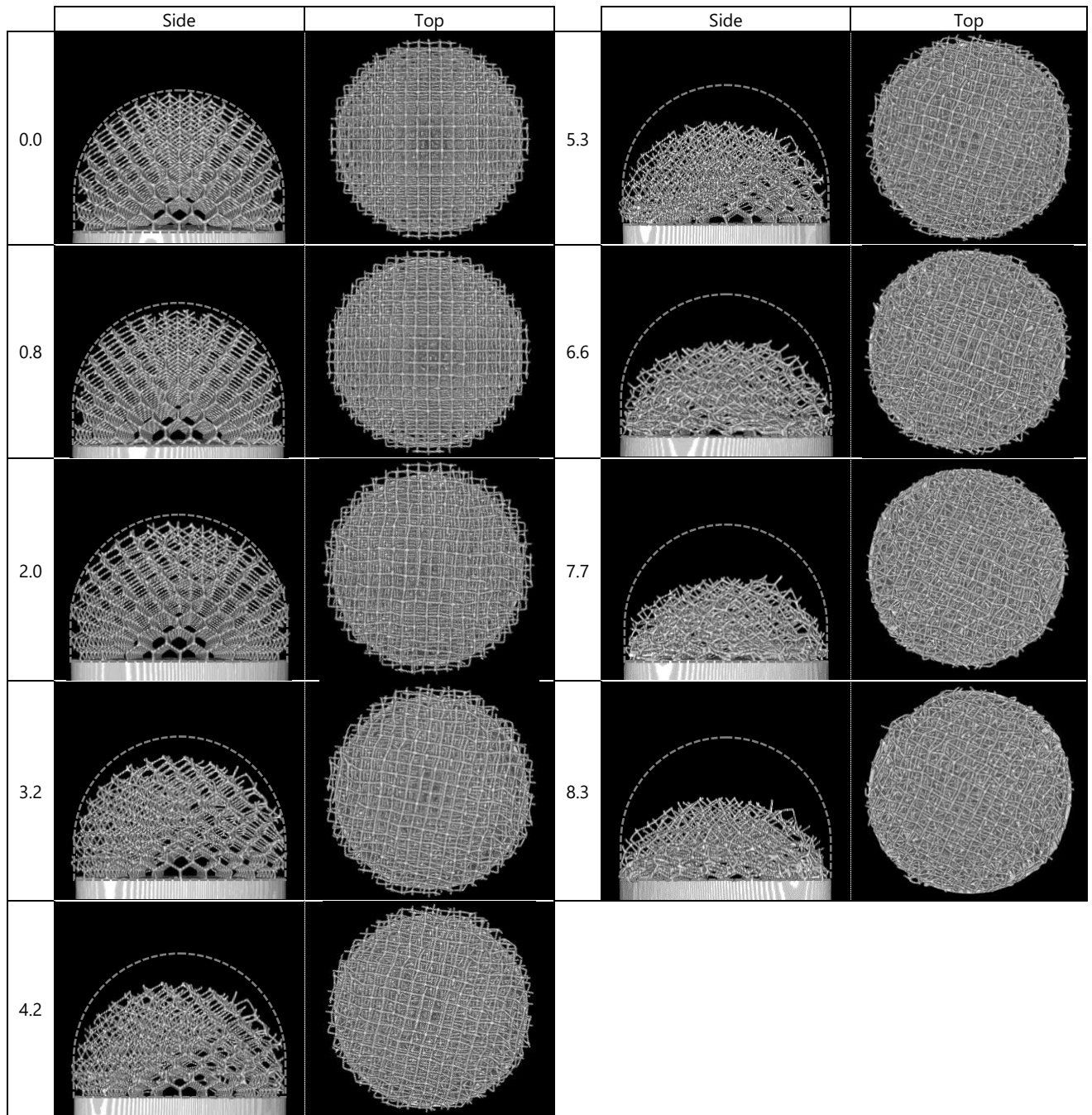


*Fig. 54* Sample 3.1.2 (structure 3, size 1) of test 3.

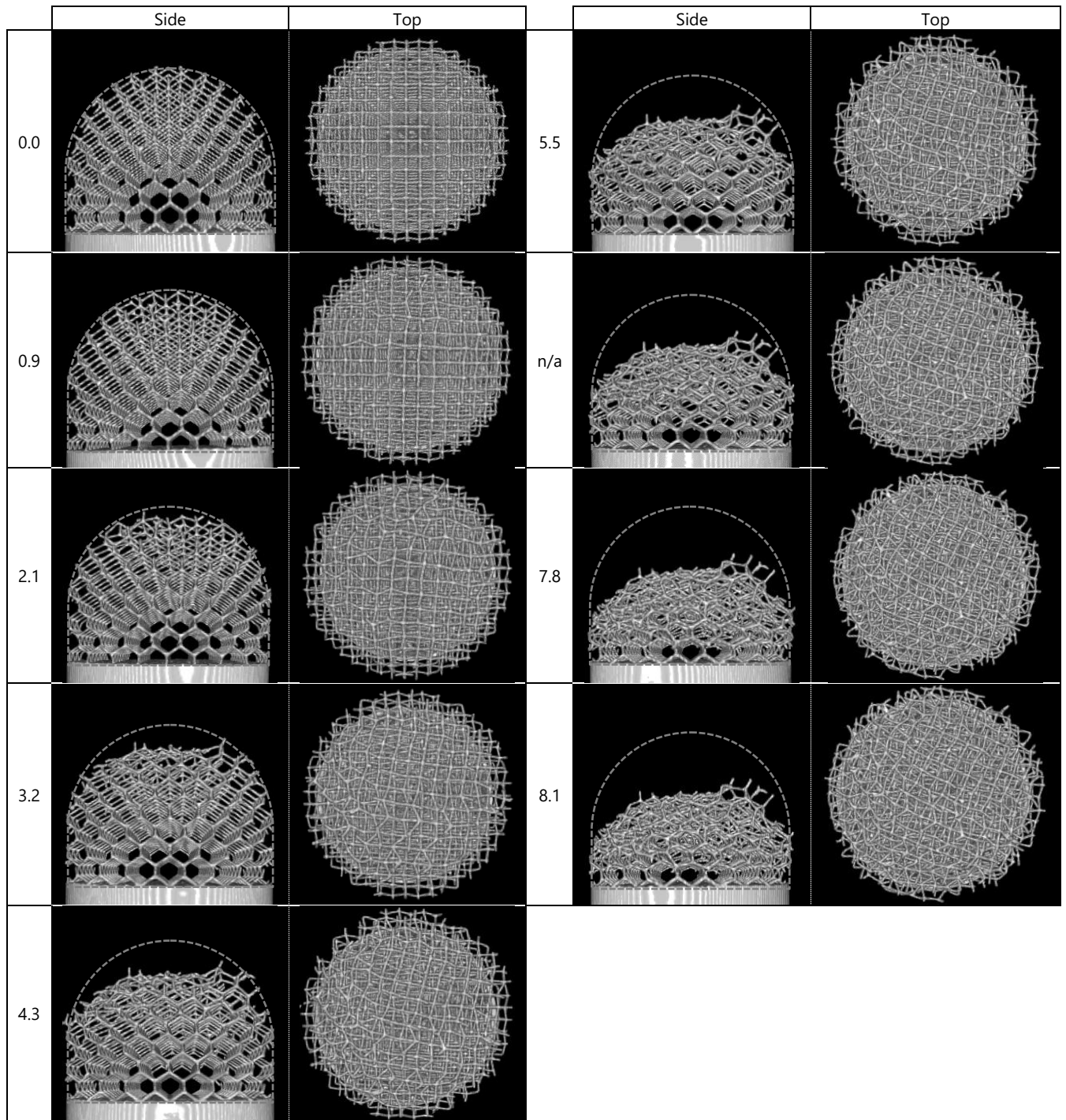


*Fig. 55* Sample 3.2.1 (structure 3, size 2) of test 3.

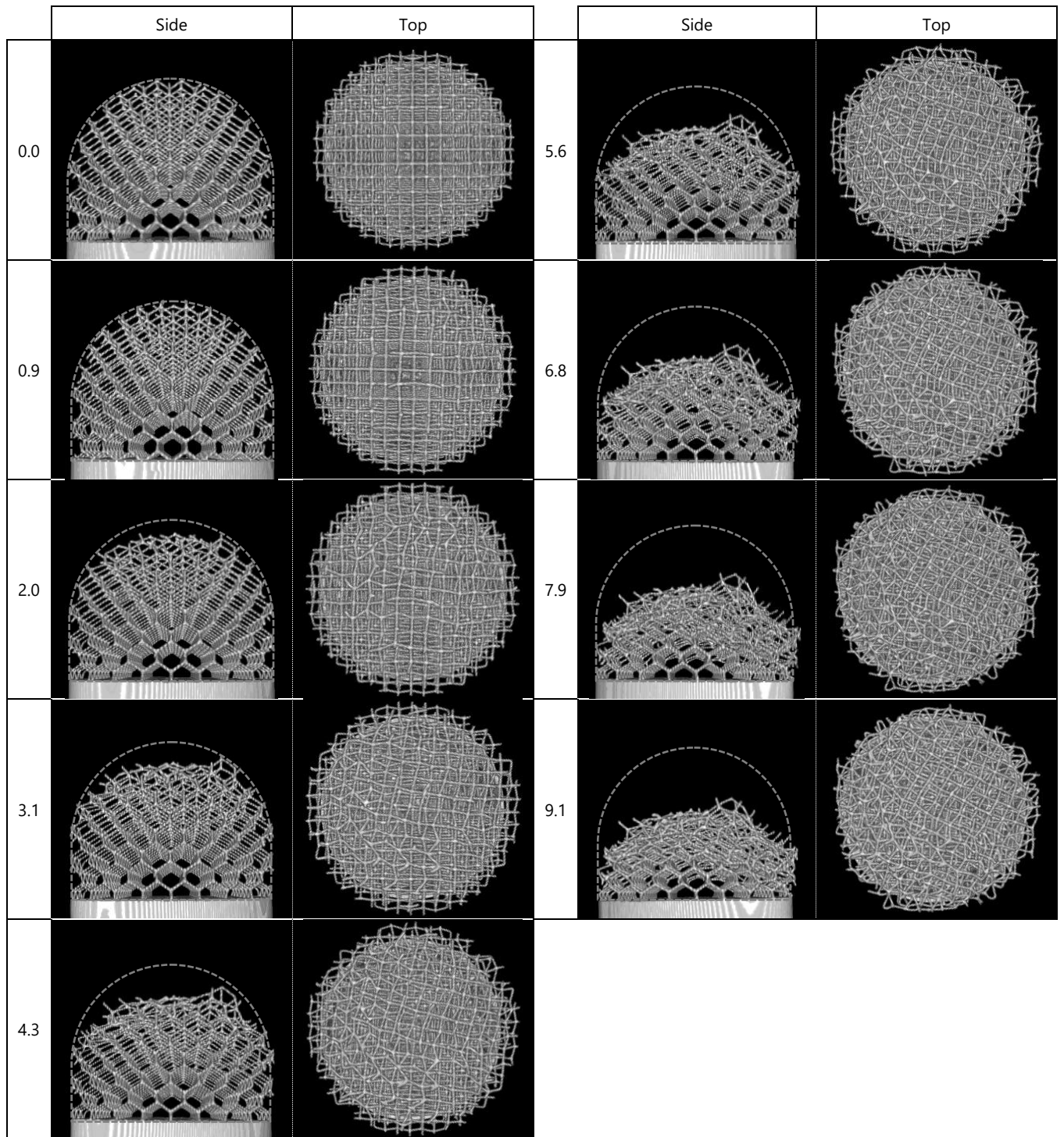


*Fig. 56* Sample 3.2.2 (structure 3, size 2) of test 3.